

Airborne Radar Testbed Radio Frequency Calibration



A Major Qualifying Project
Submitted to the Faculty of the
Worcester Polytechnic Institute
in partial fulfillment of the requirements for the
Degree in Bachelor of Science
in
Electrical and Computer Engineering
By

Alexander Corben

&

Jamie Wang

Date: 10/18/2016

Sponsoring Organization:

MIT Lincoln Laboratory

Project Advisors:

Professor Edward A. Clancy, Major Advisor

Andrew Messier, MIT Lincoln Laboratory Supervisor

DISTRIBUTION STATEMENT A. Approved for public release: distribution unlimited.

This material is based upon work supported under Air Force Contract No. FA8721-05-C-0002 and/or FA8702-15-D-0001. Any opinions, findings, conclusions or recommendations expressed in this material are those of the author(s) and do not necessarily reflect the views of the U.S. Air Force.

© 2016 Massachusetts Institute of Technology.

Delivered to the U.S. Government with Unlimited Rights, as defined in DFARS Part 252.227-7013 or 7014 (Feb 2014). Notwithstanding any copyright notice, U.S. Government rights in this work are defined by DFARS 252.227-7013 or DFARS 252.227-7014 as detailed above. Use of this work other than as specifically authorized by the U.S. Government may violate any copyrights that exist in this work.

Abstract

The Airborne Radar Testbed (ARTB) is a testing system that Group 105 at MIT Lincoln Labs is currently developing, which will be placed on a modified Twin Otter aircraft in order to demonstrate advanced radar technologies and concepts. The antenna system employed in the ARTB requires precise time synchronization during transmission in order to effectively produce and maintain control over the radiated pattern. In order to ensure successful functionality, the ARTB has a calibration module in place that can detect phase offsets in order to compensate and maintain synchronization. The concern is that it is unknown how reliable the calibration module is in detecting phase offsets accurately and consistently. During this ARTB RF calibration project we characterized the calibration system under laboratory conditions.

Statement of Authorship

All sections of this report were written and edited by both Alexander Corben and Jamie Wang. Both team members contributed equally to the project work from the design and implementation of the test system to the actual testing of the Airborne Radar Testbed RF Calibration System. Both members wrote the Abstract, Executive Summary, Introduction and Conclusions. Additionally both members edited all sections of the report, but initial sections of the report were written individually as follows:

Alexander Corben: 2.2, 2.3.1, 3.3.2, 3.3.3, 3.3, Chapter 5

Jamie Wang: 2.1, 2.3, 3.2, 3.3.1, 3.4, 3.5, Chapter 4

Acknowledgements

We would like to thank our project advisors whose generous assistance made this Major Qualifying Project possible:

Andrew Messier – Project Advisor – MIT Lincoln Laboratory

Edward Clancy – Project Advisor – Worcester Polytechnic Institute

We would also like to thank the sponsoring organization, MIT Lincoln Laboratory for supporting this project, as well as all of the members of Group 105 at MIT Lincoln Laboratory who provided valuable advice and input throughout the project period:

Jeffery Blanco

Tasadduq Hussain

Matthew Calderon

Gerald Benitz

Executive Summary

Introduction

The Airborne Radar Systems & Techniques group (Group 105) at MIT Lincoln Labs has been developing an Airborne Radar Testbed (ARTB), a testing system that will be placed on a Twin Otter aircraft, designed to facilitate end-to-end demonstrations of advanced radar concepts and technologies for Intelligence, Surveillance, and Reconnaissance (ISR) airborne radar research. The ARTB will collect raw data to aid algorithm development and demonstrate advanced RF and processing concepts.

The antenna system implemented in the ARTB is made up of Active Electronically-Scanned Arrays (AESAs). Each individual AESA panel utilizes phase shifters as opposed to time delay circuits for beam steering as they are more appealing in terms of size, weight, complexity and cost. However, utilizing phase shifter beamforming over wide instantaneous bandwidths produces beam squint impacting the accuracy of the beam significantly. To mitigate this inaccuracy, the antenna system employed on the ARTB consists of a series of six sub-array panels, each driven by a unique RF waveform generator, allowing for time delay beam steering as illustrated in Figure 1.

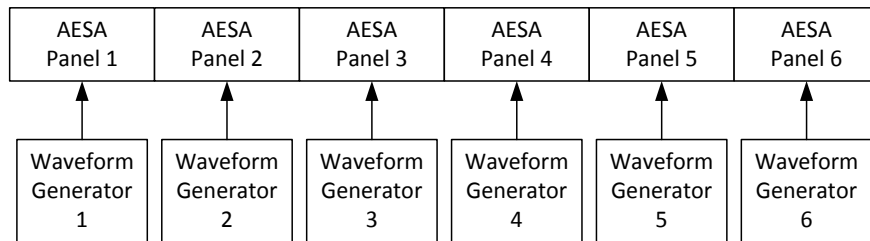


Figure 1. Sub-Array Waveform Generators

The key implementation challenge of a distributed antenna system is that all waveform generators must be precisely time synchronized to achieve a known phase at the input to each sub-array panel under any operational condition. Given that the system requires individual waveform generators for each sub-array panel, there is great potential for phase and time-delay offsets due to small differences in startup timing and clocking which cause drift between the different channels. In order to address this challenge, Group 105 has developed a calibration system for the ARTB that can determine the phase and time-delay offsets between channels and compensate for their effects. The focus of this calibration concerns the transmission end of the radar system, as it is possible given an appropriately calibrated transmission to calibrate the receive end in software using clutter.

The main goal of this project was to develop a test system, simulating the transmission portion of the testbed, in order to characterize the reliability of the ARTB RF phase calibration system. The ARTB will rely solely on the phase calibration system to compensate for offsets between each channel during transmission. Our MATLAB controlled test system consisted of two synchronized FPGAs handling waveform generation, filtering, and synchronized transmission, an upconverter bringing signals up to Ku band, components from the phase

calibration system (DUT), and two horn antennas and a receiver antenna to analyze the received power levels of the antenna patterns. We ran systematic tests at a single frequency over time, from full system resets and after applying an external phase shifter to intentionally put the system out of calibration in order to measure consistency and accuracy of the phase calibration system.

Methods

In order to investigate and characterize the reliability of the calibration system, we set five main objectives: (1) design and develop a system simulating the ARTB transmission, (2) verify that the system achieves functionality, (3) develop measurement techniques to use when testing, (4) test the calibration system of the ARTB for consistency and performance at a single frequency using two horn antennas and a receiver antenna as a feedback loop, and (5) analyze the experimental data to quantify the consistency and accuracy of the calibration unit and explore any resulting implications about the device under test.

In order to isolate and characterize the reliability of the calibration system, it was necessary to develop a system simulating the radar transmission employed on the testbed. The system was split into three main parts: waveform generation and transmission, RF components for upconversion and calibration, and two horn antennas and a power receiver acting as a feedback loop as illustrated in Figure 2.

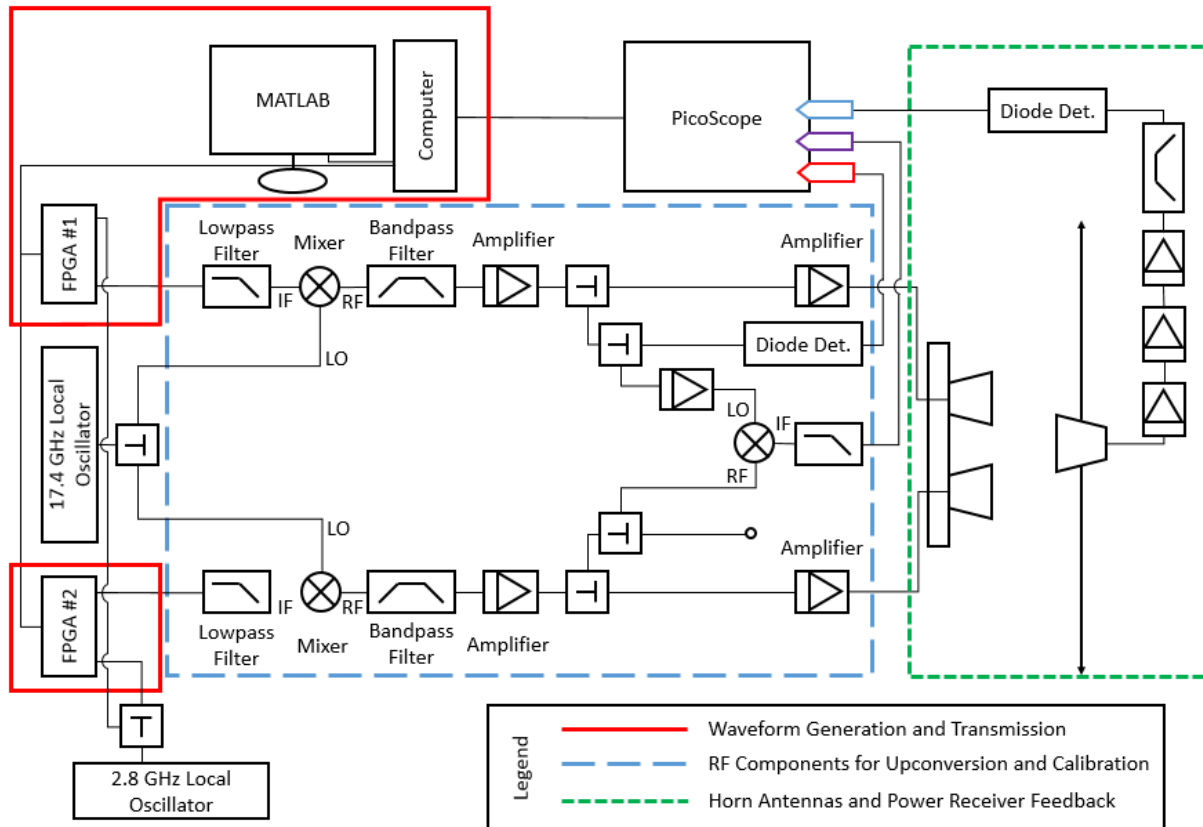


Figure 2. Overall system diagram showing FPGA hardware, upconverter and calibration RF components, and horn antennas and power receiver for feedback loop

Test Protocol

The phase calibration system of the ARTB utilized a phase detector comprised of a mixer and low-pass filter and specific calibration waveforms in order to detect phase offsets between two channels. The “reference” channel waveforms consisted of a 4μs sine wave with no phase offsets. The “test” channel waveforms consisted of a 4μs 90° phase-stepped sine wave at the same frequency. The resulting phase detector output would be four DC voltages from which the phase offset between the two channels could be calculated as illustrated in Figure 3.

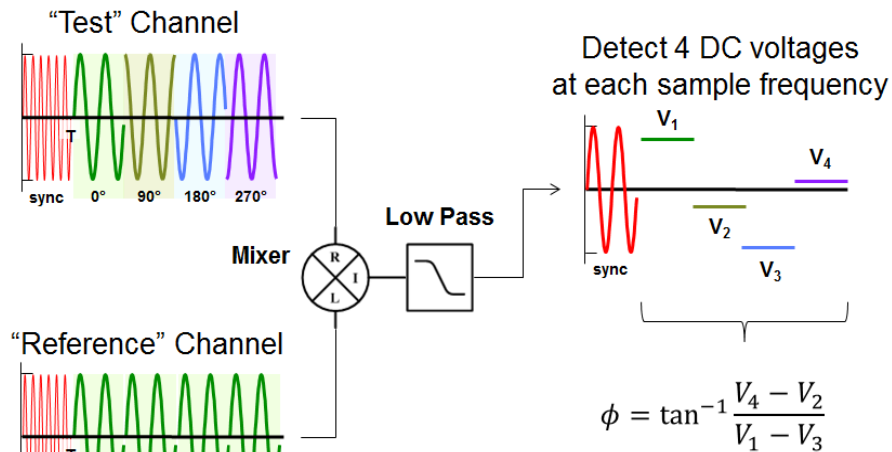


Figure 3. Calibration Waveform Theory

For the purposes of testing the calibration system, it was determined that transmitting an interferometer beam pattern would allow for the best resolution in identifying the measured beam angle from a power measurement scan taken at a receiver antenna. To create this beam pattern, transmit power measurements were taken after imposing a 180° phase relationship between the test and reference channels to produce a low power null at the center of the beam pattern.

The testing protocol for the calibration system consisted of three primary stages. In the first testing stage, a baseline null position was established to examine the consistency of the calibration measurements taken at the phase detector. This baseline null position was steered to an angle 0° off broadside by adjusting the phase difference between the two transmission channels with an analog phase shifter in the test channel, and the baseline phase detector measurements were taken 1000 times over a set of 5 full system resets to determine the measurement consistency over time.

The second stage involved intentionally adding external phase offset to the test channel via an analog phase shifter to intentionally bring the system out of calibration and move the central null away from the 0° broadside angle. The null position and phase difference was recorded with externally applied phase values from -180° to 180° and employed in the last stage of testing to verify the ability of the calibration system measurements to adequately re-align the central null position to the baseline.

The final stage of the test was to employ the phase detector measurement recorded in stage two to re-align the two signals with fractional delay FIR filtering within the FPGA system and ideally bring the null back to the same baseline measurement position. Using the phase detector feedback mimicked the actual calibration as it will occur on the actual testbed, and the power scan data provided a feedback mechanism only possible in the lab testing environment to characterize the accuracy of the calibration system's functionality.

Experimental Results

During the first stage of the testing procedure, a set of 1000 measurements was taken over 5 full system resets to examine the consistency of the calibration system's recorded data over time. The test frequency that was employed was 16.7 GHz. Figure 4 shows the results of this test, where the left plot reflects the overlaid phase detector output measurements which were used to calculate the phase relationship between the two transmitted signals, and the plot on the right is a histogram of the calculated phase differences between test and reference channels at the phase detector output.

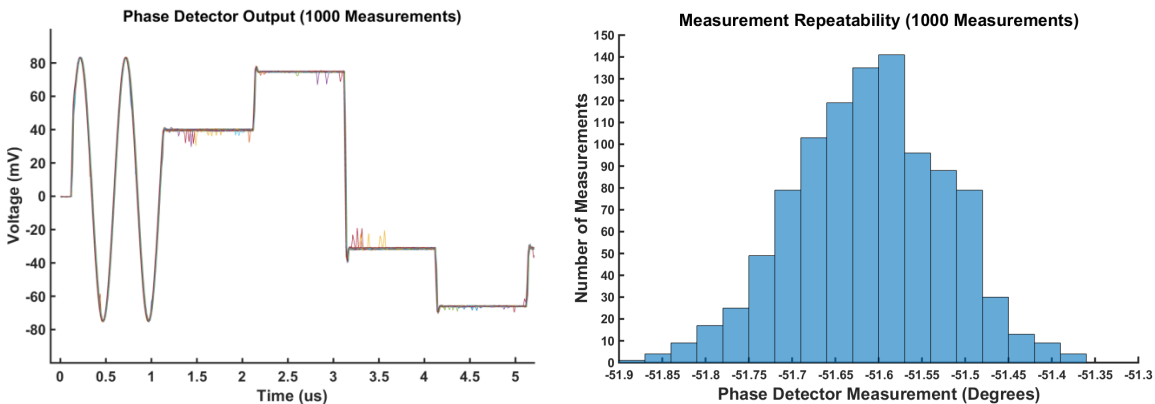


Figure 4. Calibration Module Consistency Data

Note that the mean of the histogram plot is around -51.6° rather than 0° . This offset is due to two factors: the non-ideal behavior of components within the calibration system, and the fact that the baseline measurement was taken at an off-broadside null angle close to, but not exactly at, 0° . Given the physical path lengths within the calibration system, as well as the non-ideal behavior of the components which make up the system, an additional applied phase offset is expected in the phase detector output data. This baseline offset was accounted for when attempting to re-align null positions using phase detector measurement alone.

As represented in the first stage repeatability measurements of Figure 4, the calibration system was determined to be consistent within 1° of phase difference. This 1° difference was consistent across all system resets and was observed throughout all tests performed on the calibration system. A small amount of noise is represented in the phase detector measurements, but the noise impact is eliminated by taking the average of each voltage value, as there is often just a single deviating data point in each set of measurement data.

Once this baseline was established and the consistency verified, an external phase was applied to bring the system out of calibration. In Figure 5 the blue markers represent the initial phase offset and off-broadside beam angle with this external phase applied. As expected, changing the phase relationship between the signals moved the baseline null angle. The red markers on these two plots represent the corresponding values with the re-calibrated transmission signals using the phase detector data. The phase detector output returned to within 1° of the baseline measurement, and the baseline null was correspondingly aligned back to within 0.15° of the baseline off broadside angle.

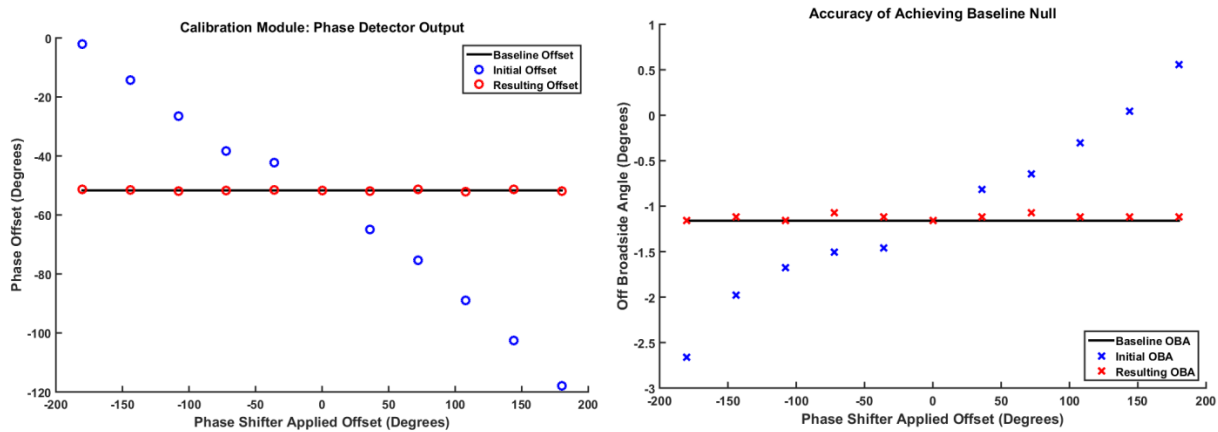


Figure 5. External Phase Offset and Re-Alignment Data

Conclusions

The gathered phase and received power measurements showed that the system was able to re-calibrate for an external offset within 1° of phase between the two channels and 0.15° of the target baseline beam angle. Given the 6 bit phase shifters employed within each of the six antenna panels, which have a resolution of 5.625° of resolution for adjusting the phase relationship between channels, the calibration system provides more than 5 times the beam steering accuracy of the antenna panels themselves. It was therefore concluded through this experiment that the calibration system designed for the Airborne Radar Testbed is not the limiting factor in the ability of the antenna system to properly steer to a desired beam angle, and as such performed within the requirements.

Table of Contents

Abstract	2
Statement of Authorship	3
Acknowledgements	4
Executive Summary	5
Introduction.....	5
Methods	6
Test Protocol	7
Experimental Results	8
Conclusions.....	9
Table of Contents	10
Table of Figures	12
1. Introduction.....	14
2. Background.....	16
2.1 Radar	16
2.1.1 Electronically Steered Arrays	17
2.1.2 Time Delay Circuits versus Phase Shifters	17
2.2 FIR Filtering.....	19
2.2.1 Ideal Fractional Delay (FD) Filter	20
2.2.2 FD Filter Approximation	21
2.3 Airborne Radar Testbed (ARTB).....	22
2.3.1 Mixer Theory	24
3. Methodology	28
3.1 Design	28
3.1.1 FPGA Design	29
3.1.2 Up-Converter	34
3.2 Verification of Test System	37
3.2.1 FPGA Design Verification.....	37
3.2.2 Upconverter Verification	37
3.3 Measurement Techniques	38

3.3.1 Calibration Waveforms	39
3.3.2 Interferometer Broadside Null	40
3.3.3 MATLAB Controlled Measurement	41
3.4 Testing Calibration System	42
3.4.1 Establish Baseline	42
3.4.2 Investigate Accuracy of Calibration Module	43
3.5 Analysis.....	43
4. Results.....	44
4.1 Verification Results	44
4.2 Experimental Results	47
5. Discussion	53
5.1 Implication of Results	53
5.2 Possible Data Concerns.....	53
5.2.1 Horizontal Linear Scan	53
5.2.2 Multipath effects	55
6. Conclusions.....	56
6.1 Measurement Conclusions	56
6.2 Future Steps	56
Works Cited	58
Appendix A. MATLAB Code for Scanning Zaber Rail and Taking Block Measurements	59

Table of Figures

Figure 1. Sub-Array Waveform Generators.....	5
Figure 2. Overall system diagram showing FPGA hardware, upconverter and calibration RF components, and horn antennas and power receiver for feedback loop	6
Figure 3. Calibration Waveform Theory.....	7
Figure 4. Calibration Module Consistency Data.....	8
Figure 5. External Phase Offset and Re-Alignment Data	9
Figure 6. Sub-array Waveform Generators (6 channels)	15
Figure 7. Overview highlighting the general blocks utilized in radar.....	16
Figure 8. Five panel array using phase shifters for beam steering	17
Figure 9. Time delay beam steering additional distance to arrive	18
Figure 10. One dimensional phased array, split into k sub-arrays, with phase shifters at antenna elements and time delay units driving each sub-array.....	19
Figure 11. Tapped Delay Line FIR Filter Implementation	20
Figure 12. ARTB 6-panel antenna (bottom left) mounting plan.....	22
Figure 13. ARTB calibration system (purple dotted box) components coupled prior to antenna system (AESAs) input.	23
Figure 14. Mixer Port Diagram.....	24
Figure 15. Double Balanced Mixer Schematic	25
Figure 16. Impact of Bias Voltage on LO Square Wave	26
Figure 17. Mixer Upconversion Operation	26
Figure 18. Overall system diagram showing FPGA hardware, upconverter and RF calibration components, and horn antennas and power receiver for feedback loop.....	29
Figure 19. FPGA block diagram inside box with UART cable for communication between MATLAB and DAC peripheral for outputting waveforms	29
Figure 20. Finite phase stepped calibration waveform for “test” channel	31
Figure 21. Magnitude response and group delay for 1/3 sample delay.....	32
Figure 22. Single sample control module, shift register for five 16 sample sets.	33
Figure 23. Upconverter Block Diagram.....	34
Figure 24. Mixer upconversion images.....	35
Figure 25. Upconverter Test Spectrogram.....	36
Figure 26. Calibration hardware in blue box with power dividers used to split transmitted signals, and sent to phase detector and horn antennas.....	36
Figure 27. Spectrogram (top) and trace (bottom) of 600 MHz sine wave converted up to 16.8 GHz, shown at peak of trace.	38
Figure 28. Picoscope three channel measurement setup.....	39
Figure 29. Calibration waveform theory	40
Figure 30. Power scan simulation for in-phase and interferometer measurements.....	41
Figure 31. Picoscope measurement of phase detector output (orange) triggered by master channel diode detector (blue)	42

Figure 32. Waveform generation and transmission (left) with laptop, two VC707 board and RF upconverter and calibration hardware in black chassis and feedback loop (right) with Zaber Motorized Rail, two horn antennas and receiver antenna	44
Figure 33. Single period of FIR filtered output for 1/3 sample delay, no delay or advance and 1/3 sample advance.....	45
Figure 34. Spectrogram at 17.4 GHz (LO) center frequency with desired 16.8 GHz RF frequency (red) and 16.2 GHz second-order spur (yellow) highly attenuated	45
Figure 35. Oscilloscope wide view of synchronized FPGA outputs for 18 μ s waveform duration of master (green) and slave (yellow) transmitted signals.....	46
Figure 36. Close view (1ns/div) of phase aligned synchronization within 1ns between master (green) and slave (yellow) transmitted signals	46
Figure 37. Received power measurement to prove interferometer concept in test environment	47
Figure 38. Baseline antenna pattern with broadside null at -1.16 $^{\circ}$ off broadside angle.....	48
Figure 39. Baseline phase detector output over 1000 700 MHz calibration waveform measurements resulting in a calculated phase offset of -51.683 $^{\circ}$	48
Figure 40. Baseline calculated transmit signal phase offset consistent within \sim 1 $^{\circ}$ over 1000 measurements	49
Figure 41. Initial phase detector output as a result of external phase offset applied by phase shifter	50
Figure 42. Initial power measurement as a result of external phase offset applied by phase shifter	50
Figure 43. Phase detector calculated transmit signal offset over 11 distinct external phase offsets applied by phase shifter	51
Figure 44. Comparison of initial null angle (blue) after applied phase shifter versus recalibrated null angle (red) based on calibration phase offset data	52
Figure 45. Horizontal Linear Scan Measurement Distance vs. Curved Scan	54
Figure 46. Overlaid return-to-baseline power scan measurements	55

1. Introduction

The Airborne Radar Systems and Techniques group (Group 105) at MIT Lincoln Laboratory has been developing an Airborne Radar Testbed (ARTB), a testing system that will be placed on a Twin Otter aircraft, designed to facilitate end-to-end demonstrations of advanced radar concepts and technologies for Intelligence, Surveillance, and Reconnaissance (ISR) airborne radar research. The ARTB will be capable of testing current and advanced radar modes such as GMTI, MMTI, SAR, ISAR, MIMO and EP¹ with built-in flexibility for future modes. It will collect raw data to aid algorithm development and demonstrate advanced RF and processing concepts.

Radio Detection And Ranging (Radar) systems are tools for target location identification which radiate electromagnetic waveforms and use the reflected energy to determine the position and/or speed of the target. The radar antenna receives some of the echoed energy from the target, and can amplify and process the returned signal to determine the location of the target in relation to the antenna (Skolnik 1.1).

Initially, radar involved mechanically-steered dish antennas, the steering of which was naturally restricted by the speed of motor and gimbal systems, and open to mechanical fatigue and wear over time as a function of the cyclic loading. An electronically-steered antenna, on the other hand, utilizes an individual electronic device behind each antenna element, which can manipulate the time delay or phase of the signal passing through it. With a computer controlling each element simultaneously, the overall beam direction and its shape can be digitally controlled rather than relying on mechanically steering the beam.

The antenna system implemented in the ARTB is comprised of Active Electronically-Scanned Arrays (AESAs). AESAs utilize phase shifters as opposed to time delay circuits for beam steering; phase shifters are more appealing than time delay circuits because of size, complexity and cost. The main difference is that time delay circuits receive the transmitted signal from a single high-power transmitter source and selectively delay a portion of the RF signal in order to form and steer the beam. In the case of phase shifters, each antenna element has its own transmit/receive module employing a phase shifter which receives a digital “command” telling the element how to delay the signal to form a particular beam. However, utilizing phase shifter beamforming over wide instantaneous bandwidths produces beam squint impacting the accuracy of the beam significantly. Beam squint refers to the case that over different frequencies, the actual beam angle progressively drifts from the expected beam angle. To combat this inaccuracy, the antenna system employed on the ARTB consists of six sub-array panels in series. Within each sub-array, the antenna elements still use phase shifters for steering. However, each sub-array panel is driven by a unique RF waveform generator as illustrated in Figure 6, allowing for

¹ GMTI refers to ground moving target indicator radar; MMTI refers to maritime moving target indicator; SAR and ISAR refer to synthetic aperture radar, utilized for airborne and spaceborne radar; MIMO refers to multiple input and multiple output radar; and EP refers to electronic protection.

either time delay beam steering or completely distinct waveforms, as in the case of multiple-input multiple-output (MIMO) operation.

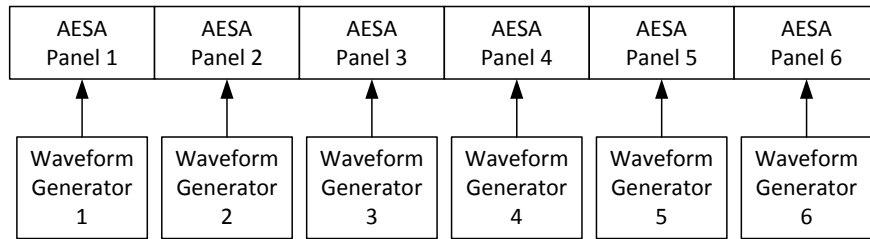


Figure 6. Sub-array Waveform Generators (6 channels)

The key implementation challenge of a distributed antenna system is that all waveform generators must be precisely time synchronized to achieve a known phase at the input to each sub-array panel under any operational condition in order to form an effective beam steering vector. Given that the system requires individual waveform generators for each sub-array panel, there is great potential for phase and time-delay offsets due to small differences in startup timing and clocking which cause drift between the different channels.

In order to address this challenge, Group 105 has developed a calibration system for the ARTB that can determine the phase and time-delay offset between channels and compensate for its effects. The focus of this calibration concerns the transmission end of the radar system, as it is possible given an appropriately calibrated transmission to calibrate the receive end using clutter, which can be handled in software. However, in determining the phase and time-delay between channels, there is some unknown offset that the calibration system itself will need to account for. Additionally, this unknown offset may vary under different operational conditions, making it necessary to properly characterize the effects of the calibration system and account for its subsequent drift such that the calibration data can be used to accurately control the resultant beam.

The main goal of this project was to develop a test system, simulating the transmission end of the ARTB in order to characterize the reliability of the ARTB RF phase calibration system. The ARTB will rely solely on the phase calibration system to compensate for offsets between each channel during transmission. Our test system consisted of FPGA design for a master and slave FPGA, handling waveform generation, filtering and synchronized transmission of waveforms. We developed an upconverter to bring signals up to Ku band, gathered components from the phase calibration system (device under test) and utilized two horn antennas and a receiver antenna to analyze the power levels of the antenna patterns. The two horn antennas provided a feedback loop that the ARTB will not have, allowing us to analyze the expected reliability of the phase calibration system. We ran systematic tests at a single frequency over time, from full system resets and after applying an external phase shifter to intentionally put the system out of calibration. With all the data collected, we analyzed and drew conclusions pertaining to the reliability of the phase calibration system.

2. Background

This chapter outlines the background information required to understand the development of our test system. First, we provide a general overview of radar, then highlight the theory and need behind development of a system for calibrating the RF calibration system on the Airborne Radar Testbed, providing an overview of the testbed itself, along with the radar techniques that it employs. Lastly, it delves deeper into a vital component of the project, the RF mixer, which was used for both frequency conversion to Ku band and phase detection.

2.1 Radar

Radar is an electromagnetic sensor for the detection of reflecting objects and can be broken up into four main subsystems as illustrated in Figure 7: transmitter, antenna, receiver and signal processor/data processing block.

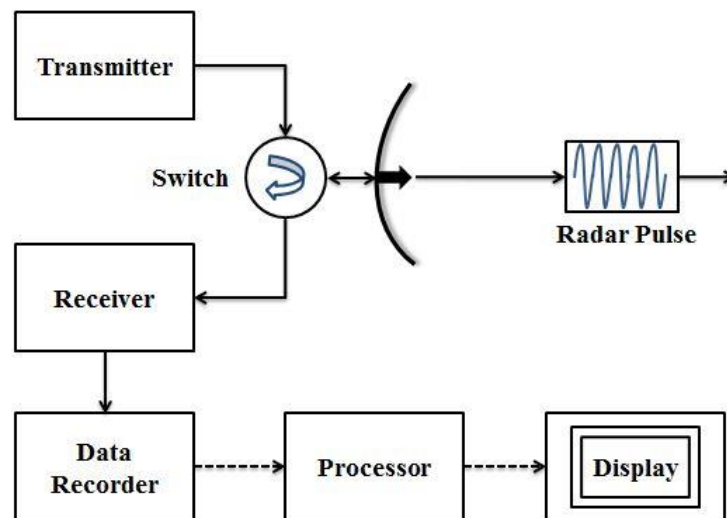


Figure 7. Overview highlighting the general blocks utilized in radar

The transmitter generates a suitable waveform for the particular functionality the radar is to serve. The antenna is the device that allows the transmitted energy to be propagated into space and then collects the echo energy on receive; it is almost always a directive antenna, one that directs the radiated energy into a narrow beam to concentrate the power as well as to allow the determination of the direction to the target. The receiver amplifies the weak received signal to a level where its presence can be detected. The signal processor might be described as being the part of the receiver that separates the desired signal from the undesired signals that can degrade the detection process. Given that radar can (generally) be broken up into these four main subsystems, it is evident that there is no single way to characterize radar. One major feature, however, that distinguishes one type of radar from another is its antenna system. The antenna can be mechanically scanned or electronically scanned to form and steer the beam; each type of antenna has its particular advantages and limitations.

2.1.1 Electronically Steered Arrays

The first generation of radar involved mechanically-steered dish antennas that were naturally restricted by the speed of motor and gimbal systems, and open to mechanical fatigue and wear over time as a function of the cyclic loading. By the 1970s, radar technology shifted to mechanically-steered planar arrays; instead of steering the beam by reflection as dish antennas do, planar arrays manipulate individual time delays into a number of antenna elements (radiators), arranged in a planar array panel. Regardless, mechanically-steered planar arrays still held heavy reliance on servomotors and gimbals that not only take a (relatively) long amount of time to steer the antenna but also suffer from fatigue applied to the components over the course of its operational time.

Phased array radars can be electrically steered, providing a faster means of beam steering and increased flexibility as the capability of rapidly and accurately switching beams permits multiple radar functions to be performed (Skolnik 13.1). Electronically steered arrays (ESAs) typically utilize time delay circuits or phase scanning to achieve beam steering.

2.1.2 Time Delay Circuits versus Phase Shifters

Beam steering can be achieved by applying the desired phase shift using phase shifters, or applying time delays which produce a frequency dependent phase shift. Consider a uniformly spaced five element linear array, depicted in Figure 8. Adjusting the phase of the signal transmitted by each element allows the collective signals to act as the signal of a single antenna, effectively forming the beam and allowing for adjustments to steer the beam as well.

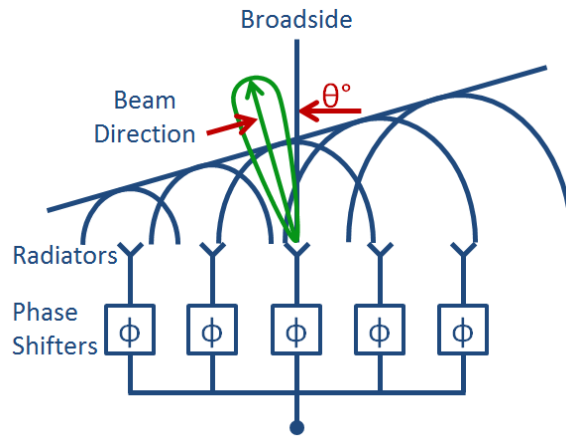


Figure 8. Five panel array using phase shifters for beam steering

By controlling the phase and amplitude of excitation to each element, the beam shape and direction can be controlled. The phase excitation controls the beam angle of the radiated pattern from the array. For example, to produce a broadside beam, $\theta_0 = 0^\circ$, the phase excitation for all elements would be $\phi_0 = 0^\circ$. Other scan angles would require a phase excitation corresponding to equation 1.

$$\phi(n) = \frac{360^\circ * d * n * \sin(\theta)}{\lambda} \quad (1)$$

where n = the n th element, d = the spacing between each antenna element (meters), θ = the desired beam angle ($^\circ$) and $\lambda = \frac{c}{f}$ where c is the velocity of propagation (speed of light: 3×10^8 m/s) and f is the frequency of the wave (Hz). If the phase shift at each element n , $\phi(n)$, is fixed, the scan angle θ becomes frequency-dependent given that wavelength λ is dependent on frequency. The change in scan angle θ as a result of change in frequency highlights the concept of beam squint, a disadvantage of phase shifters.

On the contrary, time-delay beam steering is frequency-independent; time delay units provide true time delay. For a signal transmitted at a beam angle of θ° , then according to the geometry in Figure 9 the wave must travel an additional distance $d \cdot \sin(\theta)$ to maintain the beam angle.

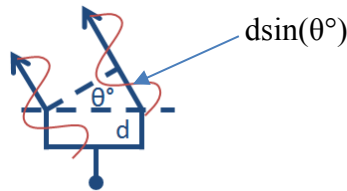


Figure 9. Time delay beam steering additional distance to arrive

Assuming the same five panel array as shown in Figure 8 with time delay circuits instead of phase shifters, the required incremental time delay at each time delay unit, $t(n)$, to achieve a beam angle θ is shown in a similar equation 2:

$$t(n) = \frac{d \cdot n \cdot \sin(\theta_0)}{c} \quad (2)$$

where n = the n th element, d = the spacing between each antenna element (meters), θ_0 = the desired beam angle ($^\circ$) and c = the velocity of propagation (speed of light: 3×10^8 m/s). The issue is that individual time-delay circuits are normally too cumbersome and impractical to be added to each radiating element (Longbrake). Phase shifters are prevalent, appealing in size, complexity and cost, but are frequency independent. Without true time delay, for wide instantaneous bandwidth signals, the beam will distort (squint) over frequency. Beam squint can be enough to steer the beam entirely off the target, resulting in a greatly reduced collected (received) signal.

To combat beam squint, the use of time delay circuits can provide true time delay beam steering. Essentially, the antenna elements of the phased array can be grouped together into a series of sub-arrays where time-delay circuits drive each sub-array, as illustrated in Figure 10.

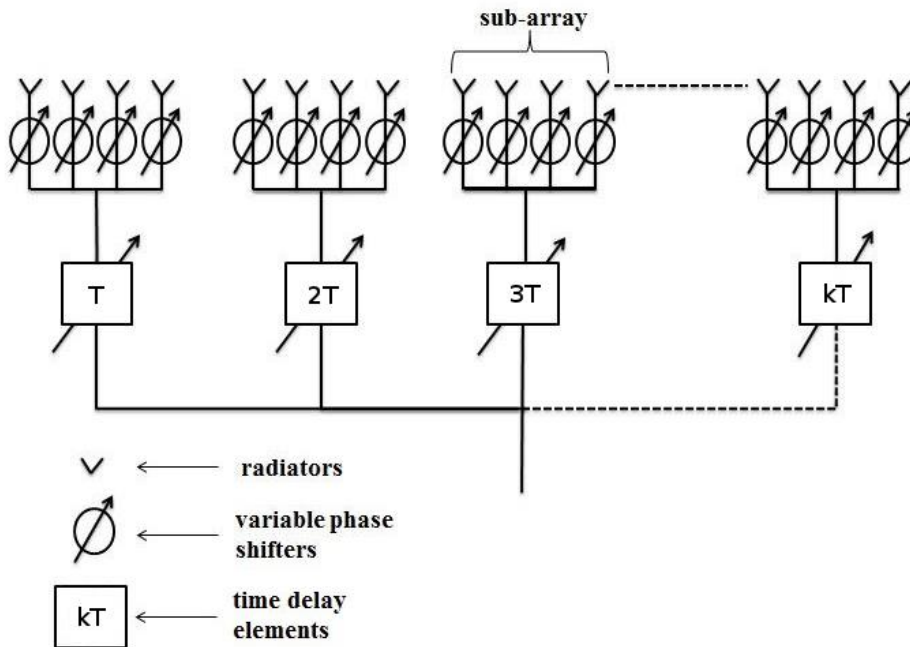


Figure 10. One dimensional phased array, split into k sub-arrays, with phase shifters at antenna elements and time delay units driving each sub-array

Dividing the phased array into a sub-arrays mitigates (but does not eliminate) the beam squint problem; each sub-array of phase shifters will have the same beam squint issue but not nearly as significantly as the beam squint that would be exhibited in a solely phase-steered array. The time delay control for each sub-array allows for true time delay beam steering of the whole antenna system. Time delay control can be achieved using switched microwave or optical networks (coaxial cables, etc.) or digital sampling and signal processing (filtering) such as a unique waveform generator for each channel (D-REX).

2.2 FIR Filtering

Finite Impulse Response (FIR) filters are generally used to attenuate the magnitude of a signal in a desired way depending on the signal's frequency. The four most common FIR filters are lowpass, highpass, bandpass, and notch filters. The basic structure to implement an FIR filter is a tapped delay line, in which a series of delays, multipliers and adders create the desired result. FIR filters are designed by selecting the set of coefficients, $a(0)$ through $a(N-1)$ where N is the order of the filter, which act as the values used by the multipliers. This basic structure is shown in Figure 11, and is represented by equation 3.

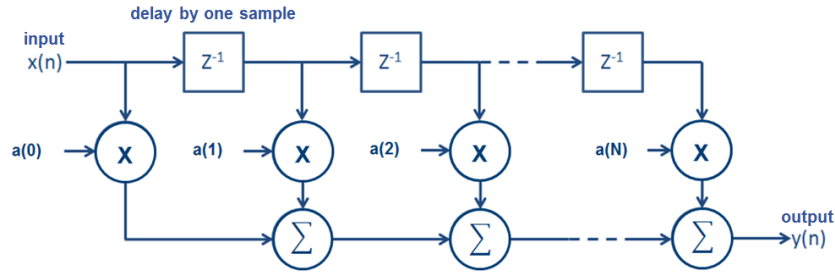


Figure 11. Tapped Delay Line FIR Filter Implementation

$$y(n) = a_0 \cdot x(n) + a_1 \cdot x(n - 1) + \dots + a_N \cdot x(n - N) \quad (3)$$

2.2.1 Ideal Fractional Delay (FD) Filter

Unlike most FIR filters, the fractional delay (FD) filter is not designed to alter the magnitude of the input signal at all. The FD filter, rather, is designed to delay a signal by a number of samples, and allows for delays smaller than an individual sample. In essence, the purpose of an ideal fractional delay filter is to interpolate a continuous signal from discrete points and resample the resultant signal with the desired time-delay offset. As discrete samples contain values for only the discrete time indices, interpolation is required in order to determine the amplitude values between discrete samples.

The Whittaker-Shannon interpolation formula, an expansion on Nyquist's sampling theorem, states that a discrete-time signal, $x(n)$, with uniform sampling period can be interpolated using equation 4 given that the continuous-time signal, $x_c(t)$, that was sampled changes smoothly between the discrete points. F_s in this function is the sampling frequency, and T is the sampling interval $1/F_s$. The $\text{sinc}()$ function represented in this equation is derived from the inverse Fourier transform of an ideal bandlimited interpolation filter, which passes all frequencies up to half of the sampling rate, the implied cutoff frequency.

$$x_c(t) = \sum_{n=-\infty}^{\infty} x(n) \cdot \text{sinc}[F_s(t - nT)] \quad (4)$$

This equation forms the basis of the ideal Fractional Delay filter; the waveform must be interpolated, shifted, and resampled to provide the necessary time delay. It is possible to combine these three components into a single FIR filter design. By doing so, the subsample values between the known discrete values can be determined. Equation 5 reflects this full operation for desired shift D (fractional samples), resulting in the desired time-shifted signal $y(n)$. Note that this filter is necessarily ideal as the infinite summation cannot be implemented in reality.

$$y(n) = \sum_{k=-\infty}^{\infty} x(k) \cdot \text{sinc}[n - D - k] \quad (5)$$

This ideal filter has a unity gain, flat magnitude response over the full range of frequencies, altering only the time delay of the signal. The phase response is:

$$\theta_{id}(f) = -2 \cdot \pi \cdot f \cdot D \quad (6)$$

The response represented here results in both phase delay and group delay constant and equal to D.

Although FD filters have linear phase response and constant phase delay, they are not traditionally considered linear-phase as the impulse response is asymmetric about the center point. Rather, the FD filter has "generalized linear phase" for the desired passband.

Unfortunately, it is impossible to realize an ideal FD filter in reality. When the desired delay is integer-valued (ie. the delay does not have a fractional component), the sinc() function is zero for every point other than at the center point, but for subsample delay the impulse response is infinite in duration, as the sampled sinc() function used for interpolation is infinitely long in both directions. As this discrete impulse response is infinitely long in both directions, the ideal filter must be non-causal for fractional delays and would have an infinite duration impulse response. Therefore, the ideal FD filter is impossible to create in reality.

2.2.2 FD Filter Approximation

The most intuitive method for approximating the ideal FD filter is to simply truncate the impulse response symmetrically about the midpoint such that it is not infinitely long in both directions. A side effect of such a truncation is frequency response ripple, referred to as Gibbs Phenomenon. Essentially, the discontinuity created by the truncation of the filter causes overshoot and ringing in the frequency domain.

There are a few different options for minimizing the effects of Gibbs Phenomenon. One could use a lowpass interpolator instead of a fullband fractional delay filter or use a reduced bandwidth with a smooth transition band function, for example. Both of these options result in a decreased bandwidth, but also decrease the amount of ripple.

Another solution is to employ a time-domain window function to provide a smooth transition to 0. As seen in this equation, the sinc function is simply multiplied by the windowing function to result in the desired response² (Poornachandra and Sasikala 7.5). Note that the windowing function $w(n - D)$ must drop-off to 0 on both sides to adequately remove the infinite sum issue, and must also be offset by D to preserve the desired filter characteristic. Equation 7 represents the impulse response of an FD filter designed with a windowing function approach.

$$h(n) = \begin{cases} w(n - D) \cdot \text{sinc}(n - D), & \text{for } 0 \leq n < N \\ 0, & \text{otherwise} \end{cases} \quad (7)$$

For the filters designed for this project, a truncated Taylor window was applied in MATLAB to the coefficient set. This window is an approximation of a Dolph-Chebyshev window which allows the Dolph-Chebyshev sidelobe ripples to drop off at the edges in the time domain, avoiding edge discontinuities, and can be expressed as:

² This is the impulse response of the filter, and as such does not include $x(n)$. The infinite summation is removed by the window which is 0 for all points outside of the desired filter order.

$$w(t) = \begin{cases} \frac{(1+k)}{2} + \frac{(1-k)}{2} \cos\left(\frac{\pi t}{\tau}\right), & \text{for } |t| \leq \tau \\ 0, & \text{otherwise} \end{cases} \quad (8)$$

where k is a value in the range of $0 \leq k \leq 1$ (Prabhu 5.2.5).

. The number of sidelobes and the sidelobe attenuation were two significant factors that had to be adjusted such that the filter maintained an appropriate bandwidth while still properly mitigating the ringing from Gibbs Phenomenon.

2.3 Airborne Radar Testbed (ARTB)

The ARTB will be mounted on a Twin Otter aircraft as illustrated in Figure 12 in order to facilitate end-to-end demonstrations of advanced radar concepts and technologies. The ARTB will be implemented in two phases; phase-1 encompasses an antenna system operating at Ku³ band single polarity with 6 channels; phase-2 expands to a 12 channel antenna system capable of operating at X⁴-Ku dual band.

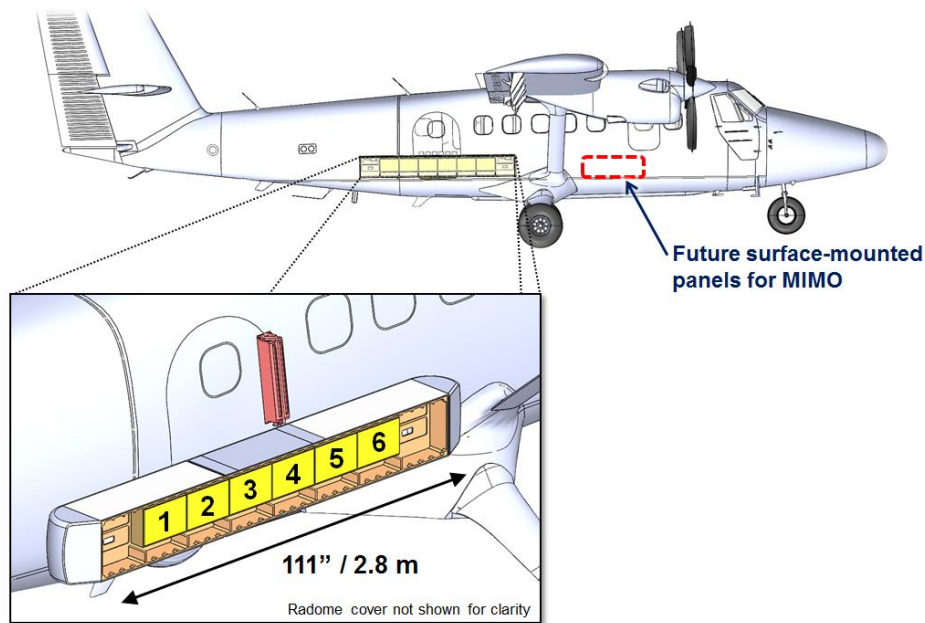


Figure 12. ARTB 6-panel antenna (bottom left) mounting plan.

System analysis indicates that the ARTB can achieve high radar performance in the expected operating environment with respect to handling clutter, platform motion, vibration and jamming. The Twin Otter aircraft will be modified in order to fit all blocks of the ARTB such as the AESA antenna system strong back (casing), digital receiver/exciter (D-REX) and processor to handle transmission and receiving signals, RF receiver/exciter and lastly data storage.

There are potential limiting factors of the ARTB, however. A primary concern is that there will naturally be some phase offset between each channel stemming from random fluctuations in phase of the local oscillator, plus additional contributions from digital-to-analog

³ Ku band (12-18 GHz)

⁴ X band (8-12 GHz)

converters and analog-to-digital converters. Furthermore, there will be a non-uniform frequency response of hardware components used in up conversion and sending of transmissions signals within the various channels, which will need to be compensated for in order to ensure effective beam steering and signal processing. In order to compensate for the phase offsets, the ARTB will employ a calibration system that can detect and adjust for phase offsets to maintain coherence, as illustrated in Figure 13.

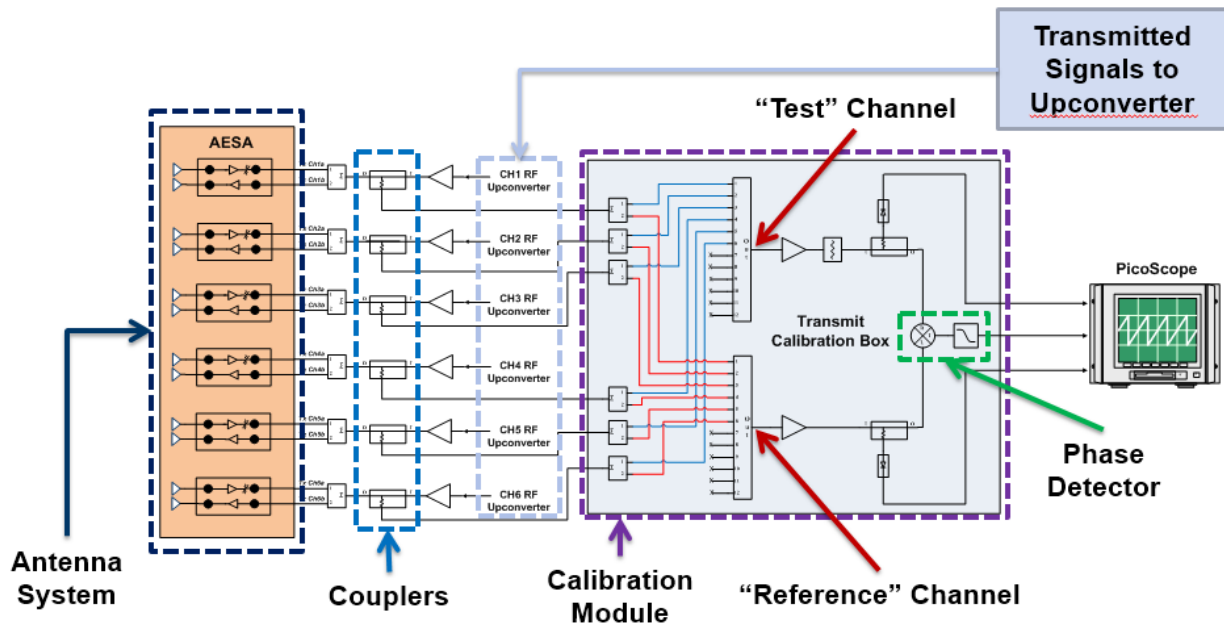


Figure 13. ARTB calibration system (purple dotted box) components coupled prior to antenna system (AESAs) input.

The waveform generator will transmit signals to upconverters, which will bring the signals up to the operating Ku band of the system. Transmission signals after the upconverter are coupled and sent to both the antenna system and the calibration system; the calibration system splits the six transmissions signals into 12, and uses a set of two switches to compare any two of the six signals at the AESAs input. The two signals are amplified and fed into a mixer to detect phase differences, the theory of which will be explained in the next section. The information is sent to the waveform generator which immediately updates phase, gain or time delay appropriately and uploads all revised waveforms to the antenna system.

However, between the varying cable path lengths directly after the splitters before the selection of the “test” and “reference” channel, and the non-linear and non-ideal components, this calibration system induces its own phase offset upon the signals that are fed into it. As a result, the reading measured by the PicoScope at the output of the mixer (used for phase detection) may not solely reflect the phase offset between channels, making the reliability of it uncertain. Thus it is necessary to properly characterize the reliability of the calibration system in order to determine whether the calibration data can be used to maintain coherence and accurately control the resultant beam.

2.3.1 Mixer Theory

A radio-frequency (RF) mixer is an active or passive three port device as illustrated in Figure 14 that, at a basic level, multiplies two different sinusoidal input signals (IF, LO) together to produce the output (RF). The cosine product identity described by equation 8 shows that an ideal multiplication will result in two different frequencies, the sum and difference, of the two input frequencies given two sinusoidal inputs.

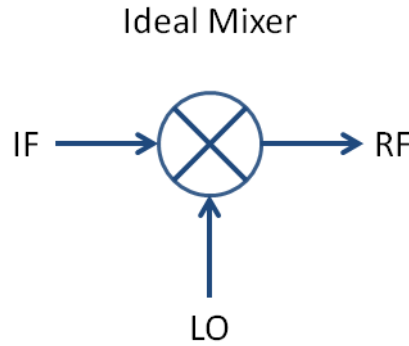


Figure 14. Mixer Port Diagram

$$IF * LO = RF = \cos(\omega_1 t) \cos(\omega_2 t) = \frac{\cos(\omega_1 t - \omega_2 t) + \cos(\omega_1 t + \omega_2 t)}{2} \quad (8)$$

For the purposes of this project, this mixer multiplication is employed for both frequency conversion and phase detection.

2.3.1.1 Double Balanced Mixer Operation

The double-balanced mixer, as illustrated in Figure 15, is a common mixer used in both frequency conversion and phase detection. There are other mixer designs in common use, but the double-balanced mixer has been chosen for this explanation specifically as it supports use as a phase detector. For the purpose of explaining the operation of the double-balanced mixer, we will observe the operation when the LO and RF ports are used as inputs and the IF port is the output signal. The mixer is not always used in this configuration, as for frequency up-conversion the RF port acts as the output and the LO and IF ports are inputs, but the behavior is similar.

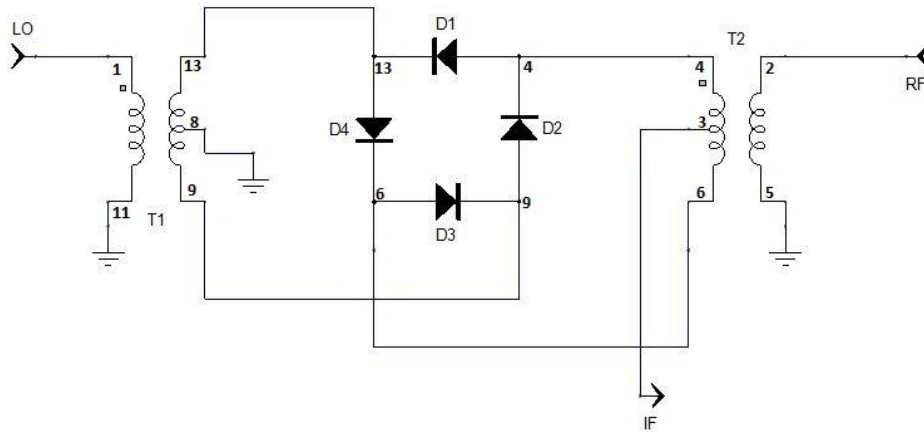


Figure 15. Double Balanced Mixer Schematic

To begin, the center-tapped transformer T1 is employed to create a differential signal from the single-ended local oscillator (LO). The diode ring essentially transforms this differential sinusoidal signal into a square wave. When the differential LO is positive, current flows through diodes D4 and D3. When these diodes are conducting, a virtual ground is created between these two diodes, as the voltage is being split evenly between them and the center-tap of the transformer T1 is tied to ground. At the same time, diodes D1 and D2 are not conducting, and can be simplified to open circuits. With D1 and D2 not conducting, one end of the transformer T2 (4) is left open-circuited and the other (6) connected to virtual ground. As a result, the application of a separate signal to the RF port passes to the IF port. Assuming a transformer turn ratio of 2:1, this signal passes through with minimal attenuation. When the differential LO signal is negative, on the other hand, diodes D1 and D2 conduct, and D3 and D4 act as open circuits. This configuration results in a situation where the opposite end of transformer T2 (6) is left open-circuited and the other (4) connected to virtual ground. Essentially, this configuration results in an inversion of the RF signal passing through to the IF port. In short, the resultant IF signal is the modulation of the RF signal with a square wave at the LO frequency. When the differential LO signal is positive, the RF input passes to the IF output normally; but when it is negative, the RF input is negated before being output to the IF port. Thus the full-wave multiplication is achieved.

This physical explanation is necessarily a simplification of the process which occurs within a double-balanced mixer, as a diode does not operate perfectly like an ideal switch. Non-linear behavior within the diodes affects the output signal and generates additional spurious frequencies beyond the two first-order images. This explanation also does not take into consideration the bias voltage of the diodes, which both decreases the magnitude of the modulating square wave, and introduces a transition interval where neither set of diodes is conducting (as shown in Figure 16), leaving both ends of the transformer open-circuited.

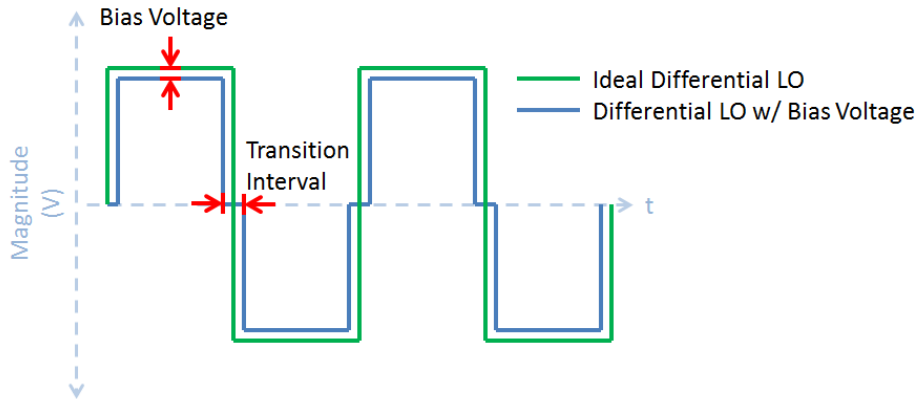


Figure 16. Impact of Bias Voltage on LO Square Wave

2.3.1.2 Frequency Conversion

The mixer's multiplying behavior makes it suitable for use converting from one frequency to another, increasing or decreasing the frequency as desired. In both up- and down-conversion, the Local Oscillator (LO) input to the mixer is driven by a continuous wave of a frequency selected such that either the sum or difference frequency is at the desired point. The output is then filtered such that only the desired output image is retained.

As mentioned earlier, however, the mixing operation is performed using non-linear elements (diodes), and these non-linearities are responsible for the generation of many additional frequencies other than the pure sum and difference frequencies. These undesired spurs must be filtered out in order to produce the clean desired frequency output. Ideally all of the input signal power is converted without any loss to the IF port. However, even an ideal mixer will lose half the input signal power (3dB) in the mixing process. The mixing process creates other unwanted spurious products as a result of diode non-linearity as well, further increasing the amount of signal power lost as illustrated by Figure 17.

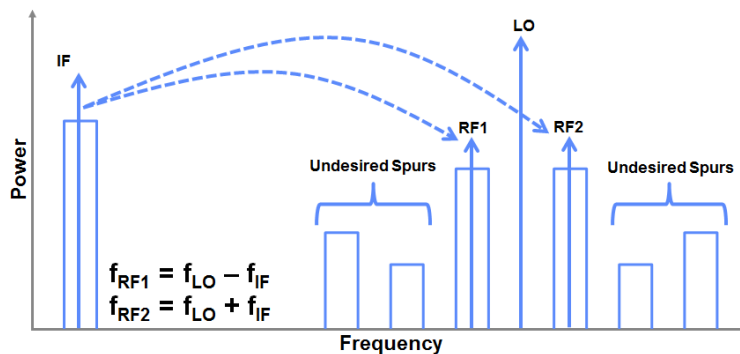


Figure 17. Mixer Upconversion Operation

2.3.1.3 Phase Detection

By the same process as the up-conversion/down-conversion mixing action, an RF mixer can be used to determine the phase difference between two different input signals if both of the input signals have the same frequency. For instance, if the signals applied to the RF and LO ports of a mixer have the same frequency ω and arbitrary phase φ , then it can be shown that, in the ideal case where the mixer operates as a pure multiplier, the resultant IF voltage will be:

$$V_o = \cos(\omega t) * \cos(\omega t + \varphi) \quad (9)$$

Using the trigonometric identity,

$$V_o = \cos(\omega t) * \cos(\omega t + \varphi) = \frac{\cos(\varphi) + \cos(2\omega t + \varphi)}{2} \quad (10)$$

Using a lowpass filter to remove the $2\omega t$ term, the output voltage will become:

$$V_o = \frac{\cos(\varphi)}{2} \quad (11)$$

As shown, the output voltage becomes a DC voltage related directly to the phase offset between the two input signals at the RF and LO ports; the output will vary as a cosine of the phase difference between the input signals making the phase offset easily derivable. Ideally when $\varphi = \pi/2$ the DC voltage output at the IF port should be zero. It is worth noting that this result reflects an inherent phase ambiguity stemming from different phase offsets corresponding to the same output voltage, i.e. $\cos(\varphi) = \cos(-\varphi)$. The phase ambiguity must be mitigated somehow in the implementation phase of a mixer as a phase detector. This phase detector application is employed by the ARTB's calibration system, the unit under test.

3. Methodology

The goal of this project investigates and characterizes the calibration system of the ARTB. Specifically, we set five main objectives to achieve: (1) design and develop a system simulating the ARTB transmission, (2) verify that the system achieves functionality, (3) develop measurement techniques to use when testing, (4) test the calibration system of the ARTB for consistency and performance at a single frequency using two horn antennas and a receiver antenna as a feedback loop, and (5) analyze the experimental data to quantify the consistency and accuracy of the calibration unit and explore any resulting implications about the device under test.

3.1 Design

The calibration system of the ARTB was the Device under Test (DUT) of our project. In order to isolate and characterize the calibration system, it was necessary to develop a system simulating the radar transmission employed on the testbed. Transmission for the system involved the creation of hardware and software for signal generation, phase alignment, transmission and radiation. To perform the transmission operations, FPGA hardware on two Virtex VC707 Evaluation Boards was developed to accept generated signals from MATLAB, adjust the relative phase of the signals, and transmit single frequency signals using a DAC. An upconverter was employed that was designed prior to the start of the project, and the resulting RF signal was transmitted via a pair of horn antennas. A power receiver captured the antenna patterns for an additional feedback loop allowing for measuring accuracy. All measurements were captured by a Picoscope controlled through MATLAB. An overall system diagram is illustrated in Figure 18.

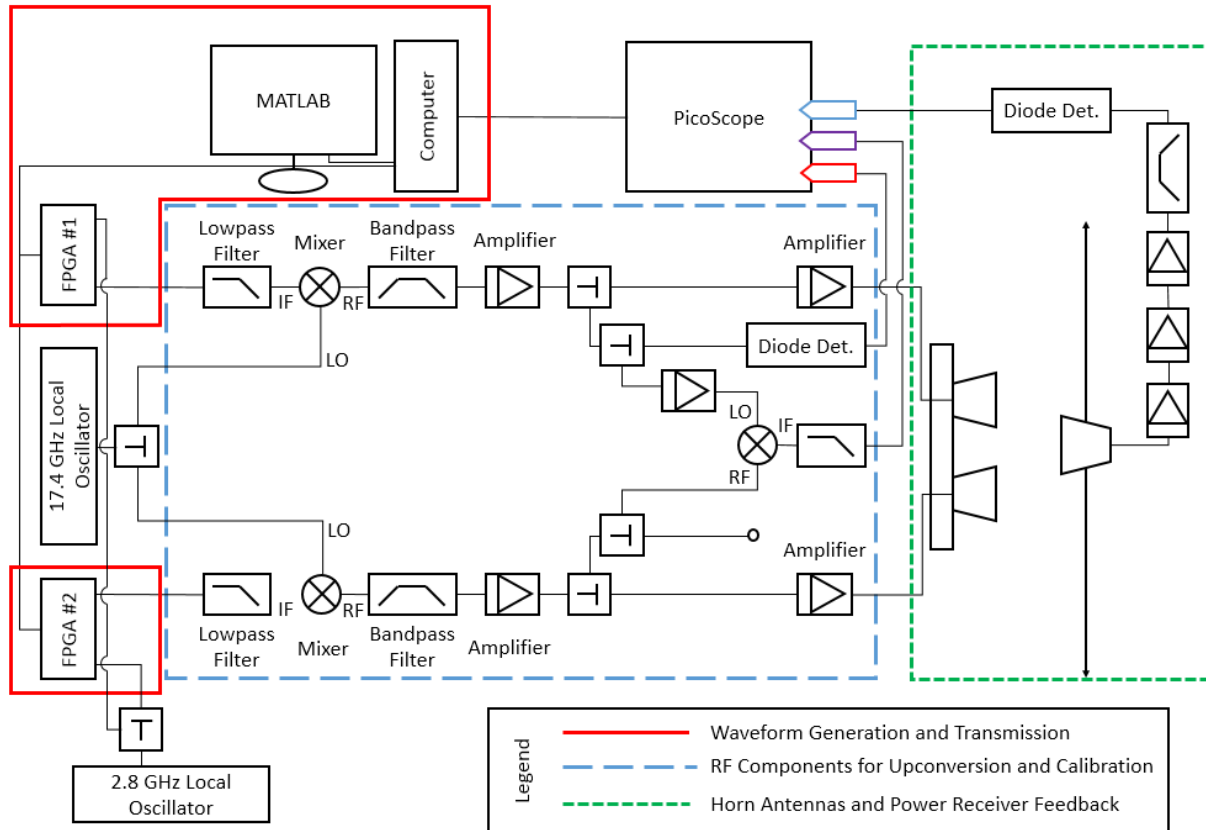


Figure 18. Overall system diagram showing FPGA hardware, upconverter and RF calibration components, and horn antennas and power receiver for feedback loop

3.1.1 FPGA Design

The largest component of the project's design involved the creation of FPGA hardware to accept the generated signals from MATLAB, adjust the relative time-delay, and transmit the signals through the DAC. In order to achieve synchronization, one master FPGA triggered the other slave FPGA. Figure 19 shows the high-level block diagram of the systems that was developed, which remained the same on both Virtex VC707 boards.

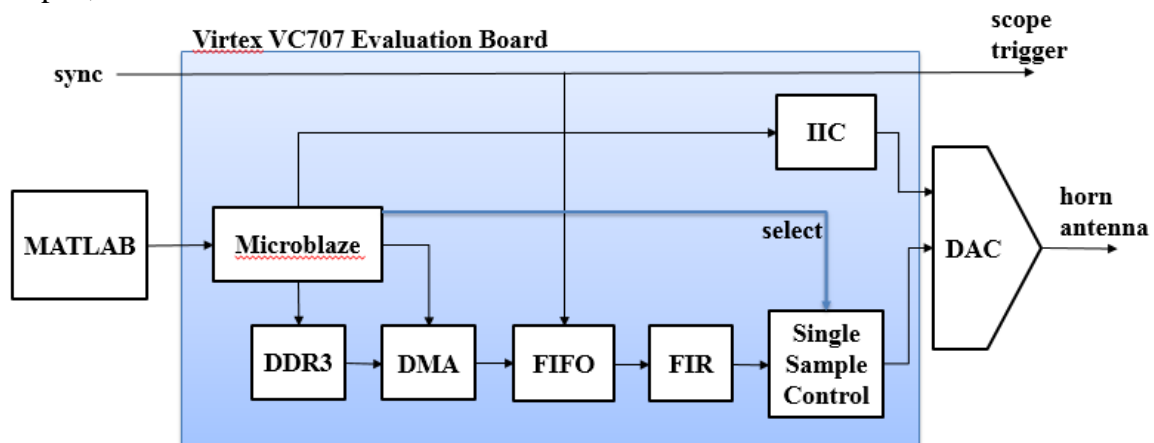


Figure 19. FPGA block diagram inside box with UART cable for communication between MATLAB and DAC peripheral for outputting waveforms

The FPGA hardware design fulfills three primary functions, the reception and storage of pre-generated waveforms, the addition of programmable delay to match the signals output by two different FPGAs, and the transmission via DAC. The reception and storage of the waveforms is accomplished via Universal Asynchronous Receiver/Transmitter (UART) transmission from MATLAB through the Microblaze, storage in DDR3 SDRAM, and a Direct Memory Access (DMA) block. A FIFO is used as a buffer to preload data from DDR3 memory in order to ensure throughput. The FIR FD and Single Sample Control filter blocks add the necessary delay, with subsample and single sample resolution, respectively. The DAC is controlled via an IIC interface. The design is then synchronized between two VC707 evaluation boards such that the waveforms can be transmitted to two different horn antennas. The two evaluation boards run simultaneously, each with the same implemented hardware design. As the DAC output defines the requirements for the rest of the system, we will first begin with an explanation of how signals are being sent from the FPGA, and will follow with a description of the system in place to meet those requirements within the chip.

3.1.1.1 Waveform Reception and Storage

The FPGA system was designed to accept any type of waveform from MATLAB such that new data could be transmitted via the antennas during the test if needed. These test waveforms take two main forms: continuous waves and calibration waveforms. Continuous waves are sine waves at specific frequencies that transmit indefinitely. The functionality was important for the experiment to account for the fact that the power receiver would take a given amount of time to scan and record the beam pattern radiated by the antennas. The second type of data used for the experiment was a finite calibration waveform. As seen in Figure 20, the calibration waveform consists of a series of “chips”: contiguous $1\mu\text{s}$ sinusoids over the set of sample frequencies. At each frequency, four of these chips were transmitted with 90° phase offset intervals so that four phase measurements could be taken (at the DUT) for each frequency. The four phase differences were sent to account for DC offset at the detector and alleviate phase ambiguity in the measurement. The method by which the detector offset and phase ambiguity is determined is further explained in Section 3.3.1. For the purposes of testing the ARTB calibration system, nine frequencies were employed in the calibration waveform, ranging from 16.6 to 17 GHz (MATLAB generated 400-800 MHz IF) in intervals of 50 MHz. Therefore, the value of N in Figure 20 is nine, and the total length of the calibration waveform is $37\mu\text{s}$.

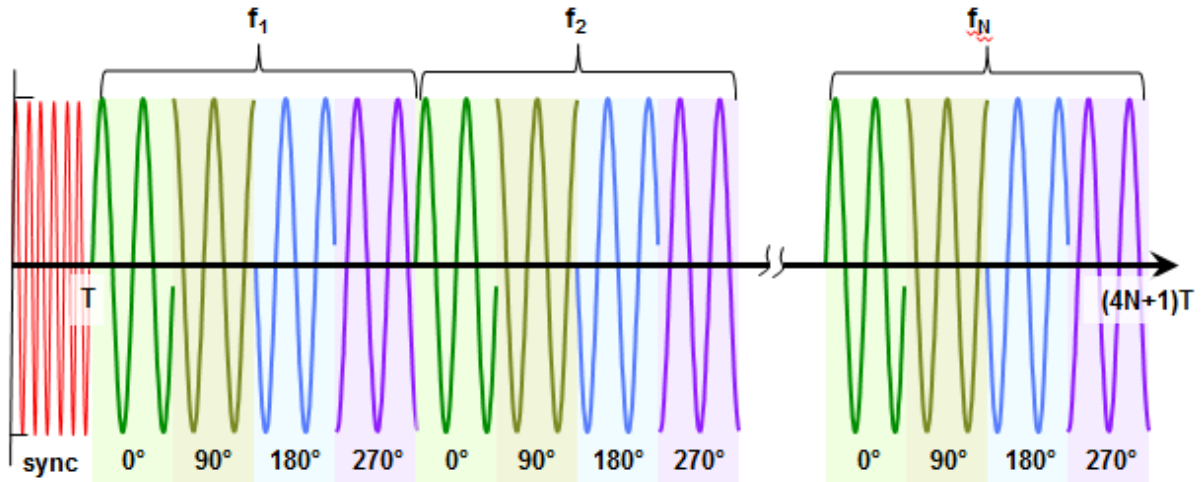


Figure 20. Finite phase stepped calibration waveform for “test” channel

Once generated, these 16-bit unsigned integer waveforms were transmitted via a serial Universal Asynchronous Receiver/Transmitter (UART) port directly from MATLAB to the FPGA. The MicroBlaze microcontroller within the FPGA stored the waveform data in DDR3 SDRAM on the VC707 evaluation board. The Microblaze then signaled a Direct Memory Access (DMA) block to begin data buffering. Before being sent through the time-delay circuitry, the data passed through a data FIFO (First-In-First-Out Buffer) which buffered the data and waited for a synchronization pulse to begin the actual transmission.

3.1.1.2 Time Delay – FIR Filter and Single Sample Control

As outlined in the background section of our report, sub-sample time delay control was achieved using Fractional Delay (FD) FIR filters. The filters generated via MATLAB using the process described in that section were loaded into a reloadable FIR filter within the FPGA. The development of filter generation code that could be easily modified allowed us to generate a variety of filters quickly during the testing process to simplify matching radiation patterns and allow for complete fine-detail control over the time delay. The filter itself was implemented with Xilinx FIR Compiler IP such that new filter coefficients could be reloaded from MATLAB at will. Figure 21 shows the flat magnitude response over the full frequency band for an example filter as well as the constant group delay. The filter shown here is one with 1/3 sample delay. Note that the group delay for the filters is in reference to a nominal delay of 12 samples, and as such the intended delay shown is 12.33 samples. The coefficients of the filters represented in the Figure 21 are converted from double-precision floats to fixed-point hexadecimal values with a sign bit and 15 fractional bits; the hexadecimal values were used in the FPGA FIR filter.

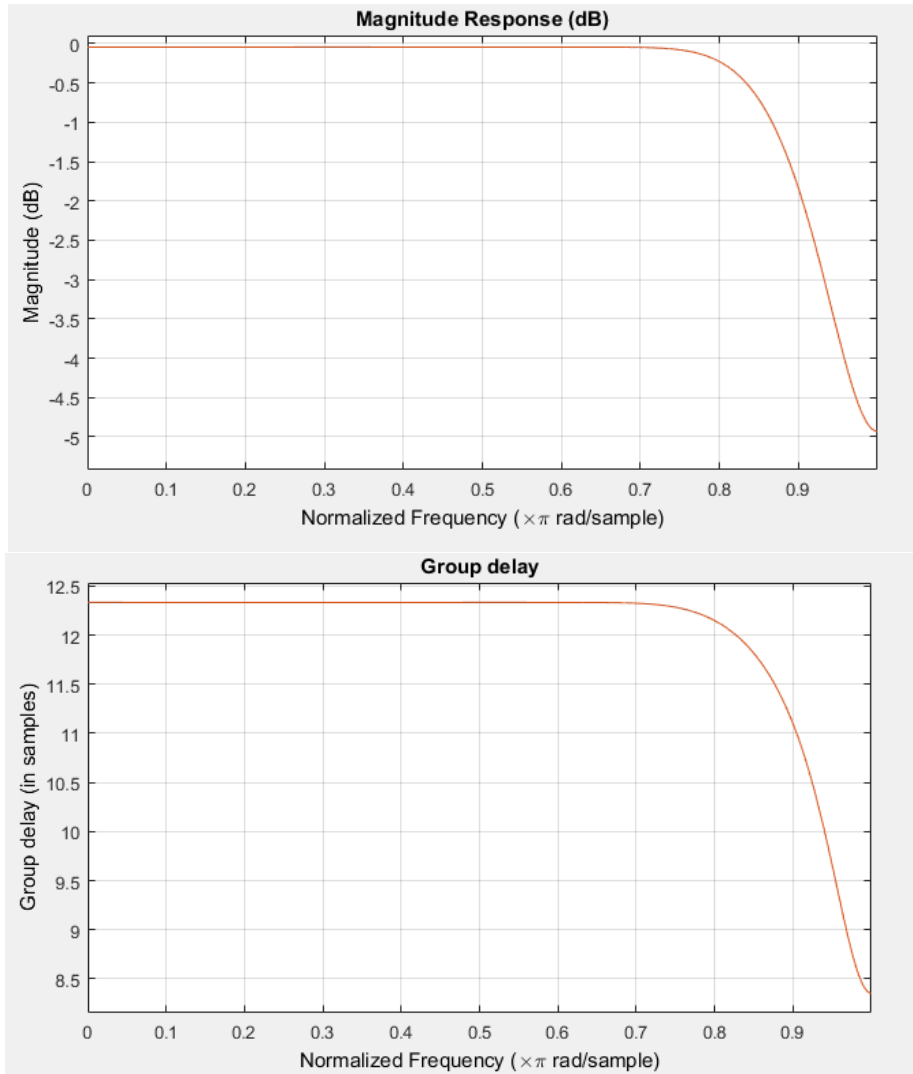


Figure 21. Magnitude response and group delay for 1/3 sample delay

Along with the fine delay adjustment from the FD filter, we also created a single-sample control module to provide the ability to adjust the output time delay with coarse, full sample resolution and allow for greater signal delay and advance. The need for a separate module stems from the timing constraint induced by the DAC sampling frequency. Given the fact that each clock tic transfers a set of 16 samples, simply delaying transmission by one clock tic would delay the output by 16 samples, not allowing for the desired resolution. The single sample control module takes in a set of 16 samples on every clock tic and moves the set into a shift register holding five sets of samples at a time. Five sample sets were chosen to provide 32 samples of delay or advance, with the ability if needed to create a 64 sample difference between the two channels. Experimental testing showed that the 32 sample amount of delay or advance was appropriate for adequately matching the waveform transmission between the two evaluation boards to within a single-sample. A selection signal sent from the Microblaze within the FPGA chooses any 16 samples within the register (not confined to input sample set borders), therefore

providing single-sample time delay control with the possibility of up to 32 samples delay or advance, as illustrated in Figure 22.

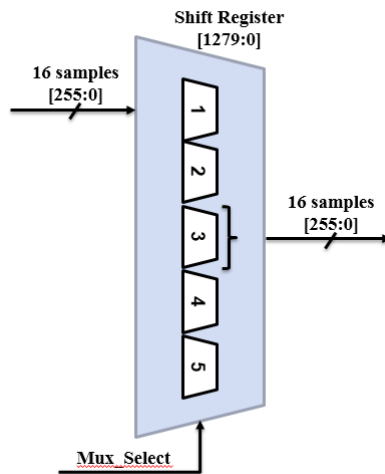


Figure 22. Single sample control module, shift register for five 16 sample sets.

3.1.1.3 DAC Sampling

The Digital-to-Analog Converter (DAC) used for our project was an Analog Devices AD9129 on an FMC160 mezzanine card made by 4DSP LLC. The DAC has 14-bit resolution and supports direct RF synthesis at a sampling frequency of 2.85 Gsps, allowing for output signals of frequencies up to around 1.4 GHz. As the IF output band from the FPGA is designed to be from 0.2 to 1.2 GHz, the 2.85 sampling frequency was determined to be appropriate.

One key challenge with operating at a sampling frequency of 2.85 Gsps is that the FPGA is unable to keep up with the fast speed sending data one sample at a time. As such, a level of parallel processing was necessary to ensure that the FPGA could properly keep up with the DAC sampling. To compensate for the speed difference, the FPGA hardware was designed such that 16 samples of data were sent to the DAC on every clock tic at 175 MHz. The DAC then takes in these 16 samples on every clock tic and transmits them sequentially at the full 2.8 Gsps speed.

3.1.1.4 Synchronization

As the FPGA hardware design was run simultaneously on two different evaluation boards, some method of synchronization was required to ensure that both waveforms were transmitted at the same time. To solve the synchronization problem, we chose to simply trigger one of the boards to transmit (the slave) with a signal from the other board (the master). The trigger from master to slave was accomplished with a cable running from two available SMA GPIO connections available on the two boards. When triggered, the MicroBlaze microcontrollers on the two evaluation boards signal the data FIFO to begin transmission through the system. The triggering method does introduce additional delay between the two boards, as it takes time for the signal to trigger the slave transmission and the clocks on the two boards will not be perfectly in phase. The transmission delay from master to slave was simple to account for however, as the design already included methods for adjusting the transmission delay. Prior to the testing period,

the signaling delay was determined between the slave and master on an oscilloscope, and the master delay was set such that the two waveforms matched as closely in time as possible.

3.1.2 Up-Converter

In the ARTB system, the DREX outputs wideband waveform centered around an Intermediate frequency (IF) of 700 MHz ~~a signal ranging from 200–1200 MHz through the DAC, but †~~The antenna system itself operates at Ku band, ~~which consists of frequencies between 12 and 18 GHz. in the region of 16 GHz.~~ The DAC output signal requires up-conversion to the necessary frequencies. For the purposes of our experiment, we used an upconverter that we designed over the summer, capable of converting 400-800 MHz to 16.6-17 GHz. ~~The 40% limited bandwidth (400 MHz as opposed to 1 GHz) was selected as the upconverter could be built with components readily available at the laboratory, and as such the lead time for obtaining components was minimized. Furthermore, †~~the 16.6-17 GHz range was deemed acceptable to draw appropriate conclusions concerning the transmit signal time-delay and phase offset as not much of the offset is attributed to the specific bandwidth, ~~(1 GHz vs. 400 MHz).~~ An HMC-T2240 Hittite Synthesized Signal Generator was employed as the 17.4 GHz local oscillator to multiply with the signal generated by the FPGA system.

The upconverter designed by the project team consists of four main RF components attached with SMA connections; a low pass filter, a mixer, a bandpass filter (image reject filter) and an amplifier as illustrated in Figure 23.

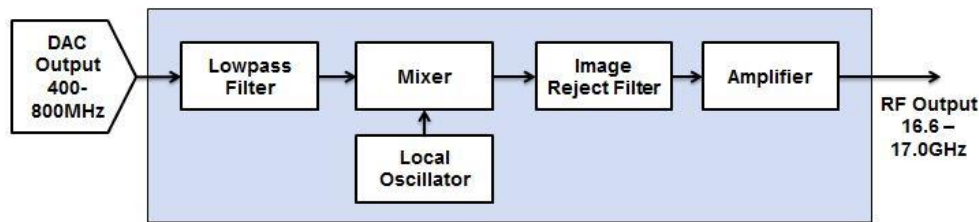


Figure 23. Upconverter Block Diagram

The lowpass filter restricts the bandwidth of the upconverted signal. The filter, a MiniCircuits 15542 lowpass filter, prevents frequency overlap between the images created by the mixer. The 3dB cutoff frequency for the chosen filter is just over 800 MHz, allowing for frequencies up to 800 MHz to pass un-attenuated.

In the upconverter application, the purpose of the next block, the mixer, is to multiply two different frequency signals (IF and LO) and produce both the sum and difference frequencies at the RF port as illustrated in Figure 24. The cosine product identity states that the product of two cosine terms results in two different frequencies, one at the sum of the two input frequencies, and one at the difference of the two, as seen in equation 12.

$$\cos(\omega_1 t)\cos(\omega_2 t) = \frac{\cos(\omega_1 t - \omega_2 t) + \cos(\omega_1 t + \omega_2 t)}{2} \quad (12)$$

The simple identity shown in equation 12 forms the basis for the upconversion process, as the goal is to transform an intermediate frequency to a higher frequency. The local oscillator in our case is simply a sinusoidal output from a signal generator at a frequency chosen such that either the sum or difference results in the desired frequency. If the IF bandwidth is not properly limited before mixing, the two generated images could overlap, interfering with each other.

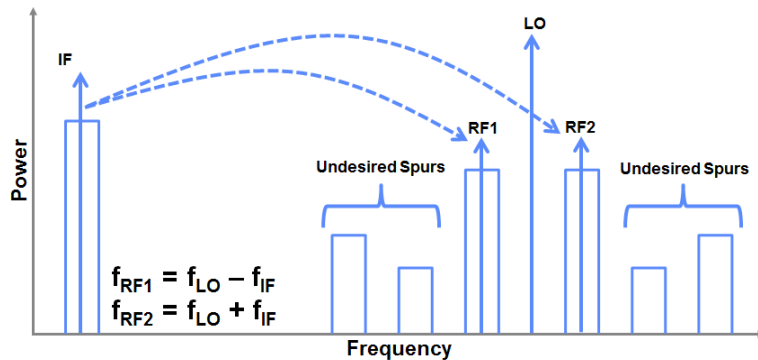


Figure 24. Mixer upconversion images

For our specific upconverter, given our IF band of 400-800 MHz, we chose a LO frequency of 17.4 GHz utilizing the equations shown in Figure 24 (above) to ensure that the images would not overlap.

$$f_{RF1} = 17.4 \text{ GHz} - (400:800 \text{ MHz}) = 16.6:17 \text{ GHz}$$

$$f_{RF2} = 17.4 \text{ GHz} + (400:800 \text{ MHz}) = 17.8:18.2 \text{ GHz}$$

At the output of the mixer, it is necessary to reject one of these images, and all of the undesired spurs, with another filter. Background section 2 of our report provides more detail. Given that the lower frequency image fell within the desired Ku band operating region, we selected a bandpass filter (K&L Microwave – 7FV10-16725/T800-0/0) with a 3 dB frequency cutoff at 16.325-17.125 GHz and attenuating below -20 dB before the 17.4 GHz LO frequency, to create the desired clean 16.6-17 GHz image using high side rejection.

With regard to higher order mixer images, the mixer in use has typical spurious suppression of around 30 dBc for the 1 RF x -2 LO frequency with a -10dBm input, and further spurs are cut off by the image reject filter that we have selected (Marki & Marki 2010). As a result, the upconverter as designed appropriately attenuates all images other than the desired frequency. The final output of the upconverter is represented in the spectrogram shown in Figure 25 with a test input IF of 600 MHz, where the desired frequency is shown in red at 16.8 GHz, and the (undesired) 1 RF x -2 LO frequency is visible as a light yellow band at 16.2 GHz. The spur shown in Figure 25 is dramatically attenuated in relation to the desired frequency, and was determined not to be an issue for the testing system as it is at only slightly higher power level than the noise floor.

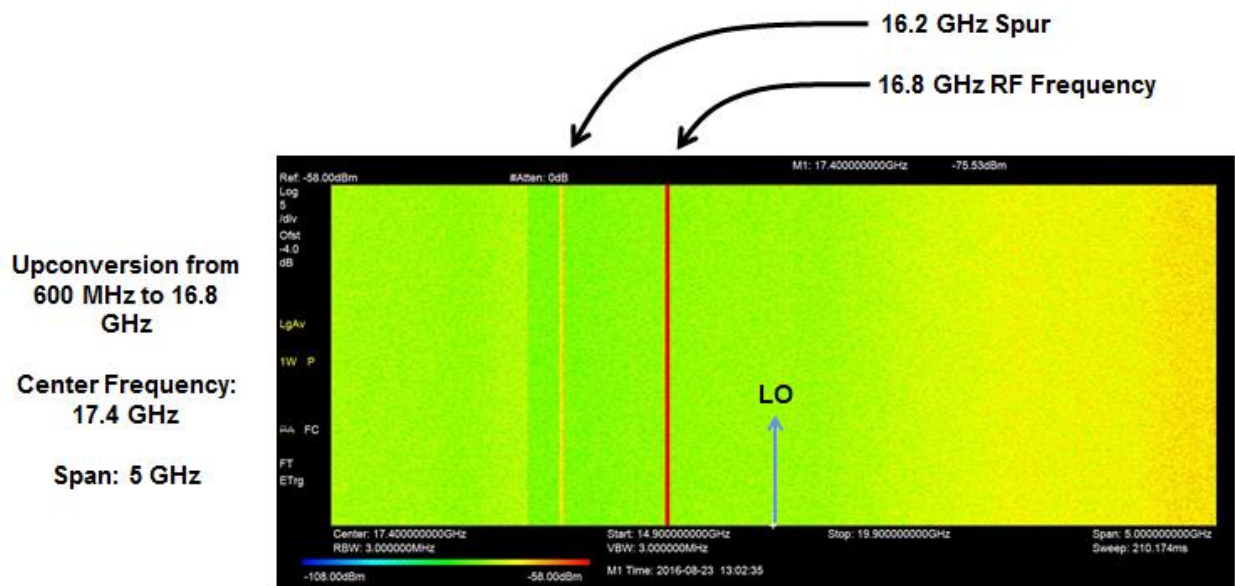


Figure 25. Upconverter Test Spectrogram

3.1.2.1 Calibration Hardware

The calibration hardware that made up the DUT consisted largely of the double-balanced mixer used as a phase detector, power dividers, and a phase shifter for intentionally putting the system out of calibration. Two horn antennas and a power receiver were utilized to provide an additional feedback loop capturing the radiated antenna patterns in order to determine accuracy of the calibration hardware as illustrated in Figure 26.

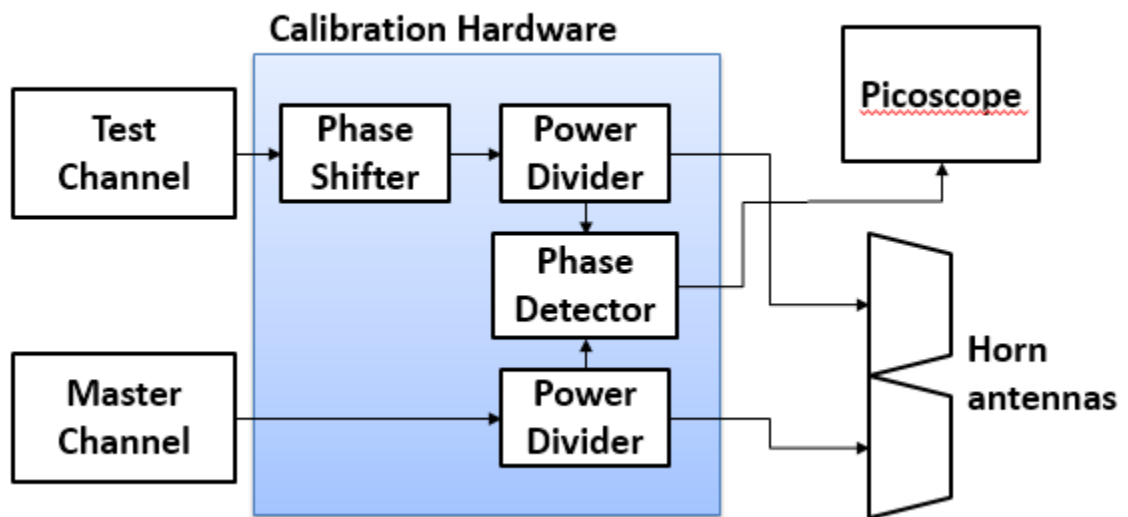


Figure 26. Calibration hardware in blue box with power dividers used to split transmitted signals, and sent to phase detector and horn antennas

Two 15dBi Ku band horn antennas (ATM – 51-441-6) were used as the radiators for the experiment; a receiver antenna was implemented to capture the power levels of the radiated antenna patterns. The phase detector, the same double balanced mixer employed in the actual ARBT calibration system (Marki M1-1020) was used such that the DUT could be appropriately characterized. A Sage Laboratories 6805-2 analog phase shifter was used to intentionally put the system out of calibration in order to measure accuracy of the calibration hardware. The power dividers used in the ARTB split the signals immediately before the antennas to send to the phase detector.

3.2 Verification of Test System

Throughout the design of our project we went through two stages of verification to ensure that our system was achieving sufficient functionality before testing. The first stage of verification was during our FPGA design period; we wanted to make sure that each module actually achieved its functionality when added to the most recent design. The second stage of verification occurred while we built our upconverter. Given that the calibration hardware was our DUT, we did not spend time verifying it outside of the actual test.

3.2.1 FPGA Design Verification

Given that the FPGA functionally stored, filtered and sent waveforms, there were multiple modules that made up the entire FPGA design. We utilized MATLAB to test each block of the FPGA design by generating sinusoidal waveforms in MATLAB that were scaled to 16-bit signed integers, for a 2.8Gsps sampling rate, varying in frequency (range of 400-800 MHz in intervals of 50 MHz) and duration. By using a universal asynchronous receiver/transmitter (UART) cable to communicate between MATLAB and the FPGA, we were able to evaluate each major checkpoint by sending a sinusoidal waveform from MATLAB to the FPGA and sequentially receiving the stored or filtered waveform in MATLAB. Given that the waveform data were scaled to 16-bit signed integers, we used big endian storage on both the MATLAB and FPGA side allowing for plotting the transmitted and stored or filtered waveforms. In order to test the sending waveforms over the DAC, we used an oscilloscope to examine the output analog waveforms.

3.2.2 Upconverter Verification

Similar to the testing of our FPGA design, during our design of the upconverter, we ran multiple tests beginning with each individual component of the full upconverter. Initially, given that we were not ordering components but rather gathering components at our disposal, we used a Network Analyzer to visualize the response of different components. After finding components (lowpass filter, mixer, bandpass filter, and amplifier) that theoretically fit our upconversion need, we ran simulations in Genesys⁵ to ensure that the upconverter would work. After running simulations in Genesys, we built the upconverter and used a spectrum analyzer to observe the converted signals ensuring that the upconverter was bringing the IF band signal (400-800 MHz)

⁵ Genesys is an RF design program.

up to Ku band with low jitter and high attenuation of unwanted spurs as desired. As we did with each block of the FPGA design, we added the upconverter to the most recent FPGA design, generated and sent a sine wave from MATLAB through the system and observed the spectrum analyzer to ensure that the full FPGA and upconverter system were working together, as illustrated in Figure 27.

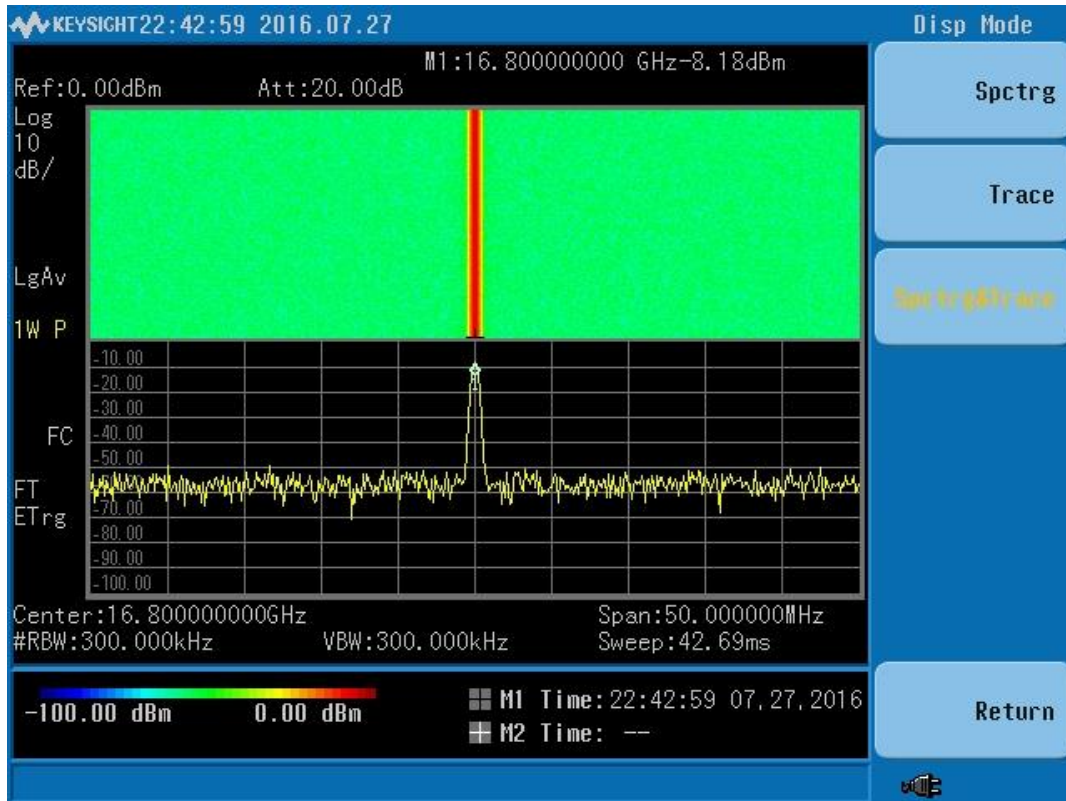


Figure 27. Spectrogram (top) and trace (bottom) of 600 MHz sine wave converted up to 16.8 GHz, shown at peak of trace.

3.3 Measurement Techniques

We utilized a Picoscope controlled by MATLAB to measure and record output data. The two sources of feedback measurement data for the experiment were the phase detector measurements from the calibration module’s phase detector output, as well as the receive power scans taken at a distance of 2 meters from the transmission antennas. The master channel diode detector output was sent to a third channel on the Picoscope; the diode detector output was an envelope of the transmitted signal acting as a trigger. The Picoscope measurement setup is depicted in Figure 28.

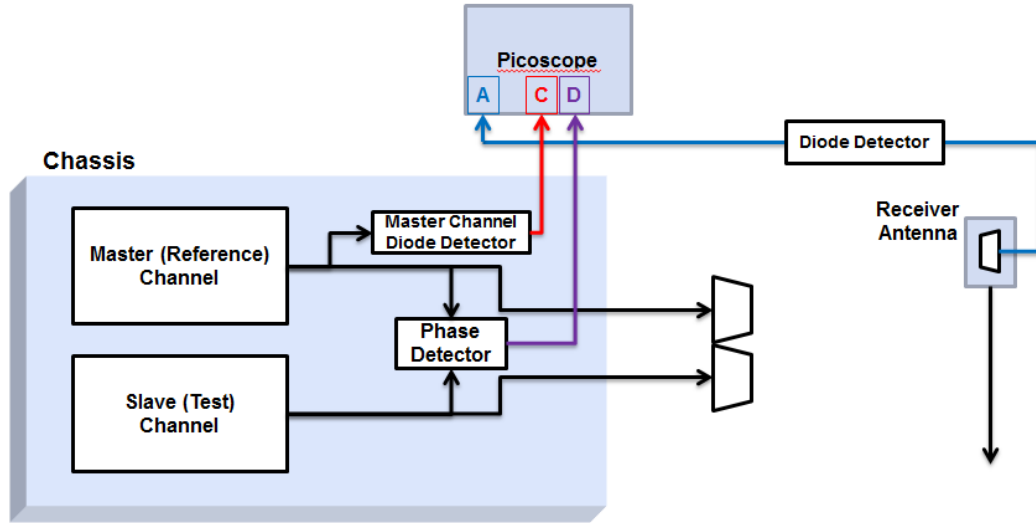


Figure 28. Picoscope three channel measurement setup

There were three main measurement techniques. The phase detector relied on very specific calibration waveforms in order to calculate the transmit signal phase offset between the two channels. The received power measurement scanned a purposely induced interferometer pattern, described in detail later in this section. Lastly, MATLAB was used to control all measurements on the Picoscope.

3.3.1 Calibration Waveforms

The phase detector had the ability to detect transmit signal phase offsets with specific calibration waveforms. The calibration waveforms were essentially five $1\mu\text{s}$ chips, that varied slightly between the master (reference) channel and slave (test) channel as illustrated in Figure 29.

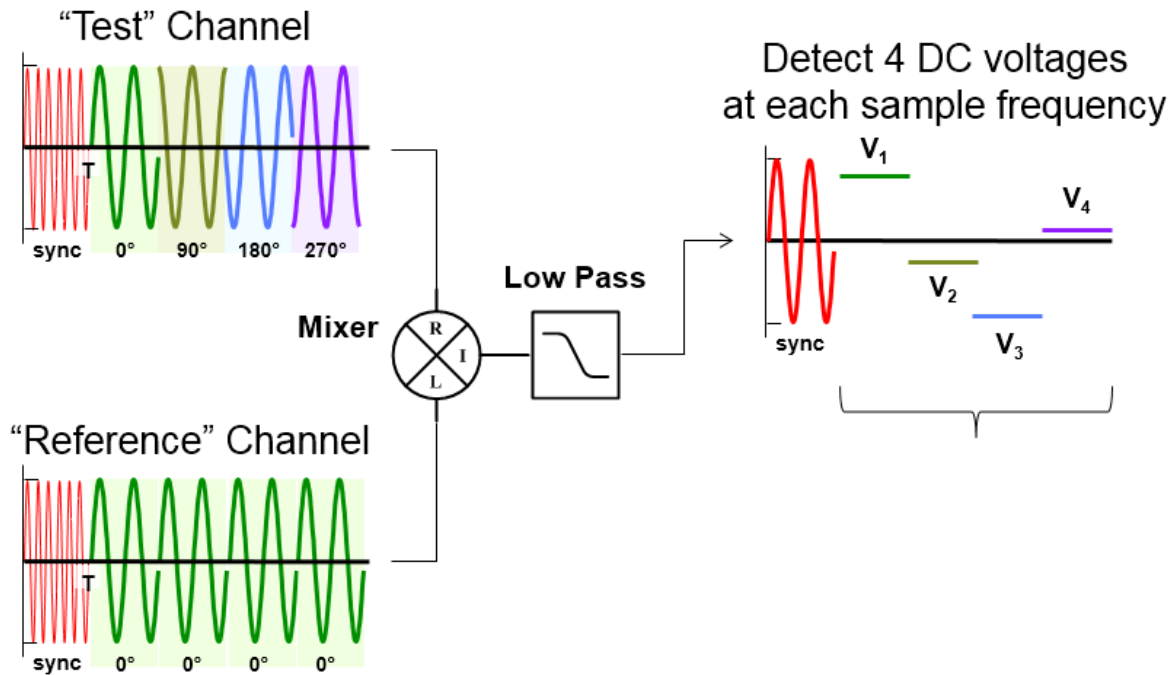


Figure 29. Calibration waveform theory

For the untouched “reference” channel, we sent a normal 5µs 700 MHz sine wave with no phase offset. For the “test” channel, we sent five distinct 1µs chips. The first “sync” chip was a 702 MHz sine wave with no phase offset; the next 4µs chips were a 700 MHz 90° phase stepped sine wave. The two MHz difference between the sync chips would act as a trigger on the Picoscope by resulting in a low frequency sine wave. The next 4µs chips would result in four DC voltages, from which we determined the transmit signal phase offset between the two channels using equation 13.

$$\phi = \tan^{-1}\left(\frac{V_4 - V_2}{V_1 - V_3}\right) \quad (13)$$

3.3.2 Interferometer Broadside Null

The main reason for measuring the received power was to track the beam angle of the antenna pattern; the feedback of the antenna pattern gave us the ability to determine whether the system was in-phase. Relying solely on the calibration module without prior characterization, the phase detector output did not accurately reflect the true offset of the system. We determined that the easiest way to track the beam angle would be to induce an interferometer; an interferometer occurs when two signals are 180° out of phase in relationship to each other. The destructive interference between their antenna patterns results in a deep power null at the center of the beam pattern, referred to as a broadside null. Figure 30 demonstrates the fact that simulating an interferometer using the out-of-phase power data was easier and more accurate than using the in-phase data. For the in-phase data, the slope of the power measurement was very low, and as such accuracy of deriving the beam angle was correspondingly low, but with the out-of-phase data, the slope was much more dramatic, making it easy to derive the beam angle with high accuracy.

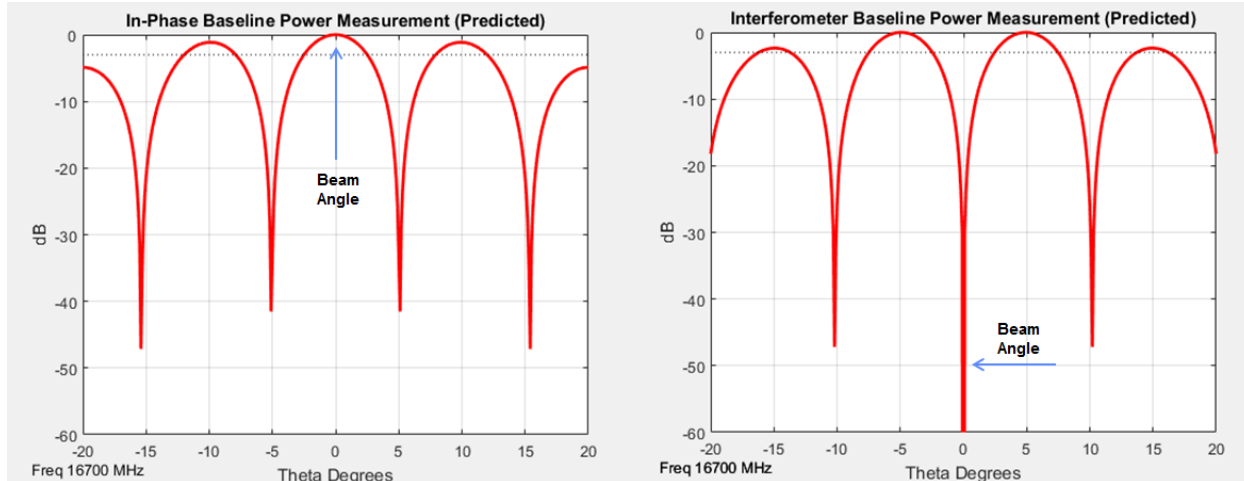


Figure 30. Power scan simulation for in-phase and interferometer measurements

3.3.3 MATLAB Controlled Measurement

To record the received power measurements, a Zaber Technologies A-LST0750B-E01 motorized linear rail was controlled via MATLAB to step through a 1.5 meter horizontal linear scan at the desired scan resolution. The MATLAB code was designed to allow user-defined resolution such that initial verification measurements could be run quickly with low resolution for easy iteration and final measurements could be run at higher resolution for full detail.

At each step of the linear scan, the MATLAB code configured the PicoScope for a 5.5 μ s block data capture, triggered on the rising edge of the waveform envelope recorded at Channel C in Figure 28. The envelope signal was created using the master channel diode detector, which received the calibration waveform from a splitter before the phase detector mixer for the purposes of triggering. Therefore, once triggered by Channel C, the PicoScope captured the full 5 μ s calibration output from the phase detector, as well as a block data capture of the received power at the receiver antenna. Once a block data capture was recorded via the PicoScope and stored within MATLAB variables, the rail moved to the next position and configured the scope for the next data capture. A sample Picoscope measurement is pictured in Figure 31, of the master channel diode detector trigger as well as the recorded phase detector output. The MATLAB code for scanning the Zaber rail and taking block measurements from the Picoscope is shown in Appendix A.

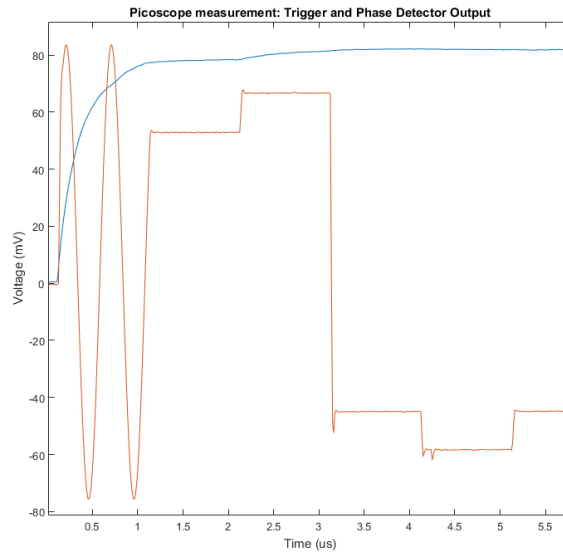


Figure 31. Picoscope measurement of phase detector output (orange) triggered by master channel diode detector (blue)

A result of this measurement method was the ability to take both phase detector measurements and receive power measurements simultaneously. Furthermore, as a block capture was taken for the three PicoScope channels for the duration of the calibration waveform, each measurement position provided four sets of received power data for each of the four signal phase relationships. We chose to take the received power data when the two channels had an 180° phase relationship between them, in order to collect the received power of the interference pattern and track the broadside null.

3.4 Testing Calibration System

Once we had verified that our test system achieved functionality, and we had measurement techniques in place, we went to the test facility to run the actual test on the calibration module of the ARTB at a single frequency of 700 MHz (16.7 GHz at Ku band). The testing protocol had three main steps: (1) establish a baseline null angle and transmit signal phase offset, (2) utilize an analog phase shifter to intentionally put the system out of calibration, and (3) based on transmit signal phase offset data from the calibration system, adjust the “test” channel and measure the resulting interference pattern and transmit signal phase offset.

3.4.1 Establish Baseline

The first step of our test protocol was to establish a baseline null angle and transmit signal phase offset. We left the master FPGA (“reference” channel) untouched, and only tuned the slave FPGA which became our “test” channel. We took an iterative approach to establish the baseline null position. First we took a 1D horizontal scan of the interference pattern utilizing the technique described in Section 3.3.3; if the broadside null wasn’t close enough to boresight (0°) we tuned the “test” channel and took a 1D horizontal scan of the interference pattern again. We measured the broadside null angle visually from the MATLAB plot of the horizontal power scan,

finding the lowest power level and recording its respective angle. Once the broadside null was within a few degrees of boresight and we had established our baseline null angle, we investigated consistency of the calibration module. In order to investigate consistency, we sent the calibration waveforms described in Section 3.3.2 and recorded the phase detector output of the calibration module over five full system resets (power off and on all power supplies to amplifiers, VC707 boards, etc.) with 1000 measurements; MATLAB calculated the transmit signal phase offset using equation 13, based on the average of each DC voltage.

3.4.2 Investigate Accuracy of Calibration Module

Once we had established a baseline null position and transmit signal phase offset, we wanted to investigate the accuracy of the calibration module. We first applied an intentional phase shift to the “test” channel that put the system out of calibration. Next, we recorded the interference pattern and calibration phase detector output; we only recorded the interference pattern to ensure that the baseline null position had shifted. We then recalibrated the system based solely on the calibration phase detector output and lastly, recorded the resulting interference pattern and calibration phase detector output. The figure of merit was the accuracy between the baseline null angle and the recalibrated null angle. We applied 10 different phase shifts between -180 to 180° with an analog phase shifter, recording the initial and resulting null angle and transmit signal phase offset for each phase shift.

3.5 Analysis

The final objective of this project was to make sense of all the data we had collected, drawing insight into the behavior of the calibration system. The data collected fell into two categories, broadside null angle in terms of off broadside angle ($^\circ$) and calculated transmit signal phase offset ($^\circ$). In order to analyze the consistency aspect of the calibration module, we calculated the mean and range of the calculated transmit signal phase offsets from Section 4.4.1. We utilized MATLAB to generate histograms highlighting the consistency of the phase detected offsets; we generated scatter plots comparing the initial and resulting null angle and calculated transmit signal phase offset to analyze the accuracy of the calibration module.

4. Results

The test system designed during this project required verification prior to data collection. Preliminary verification tests were run for the FPGA design, upconverter hardware and antenna/receiver feedback loop. Once the test system was determined to be operational, we conducted our experiment. The data collected consisted of 1D horizontal scans of received power from the two horn antennas as well as phase detector voltage output over time; all of the data were collected by a PicoScope which was controlled by MATLAB, making it easy to analyze directly from MATLAB. Figure 32 shows pictures of the entire test setup from waveform generation to our horn antennas and receiver antenna feedback loop.

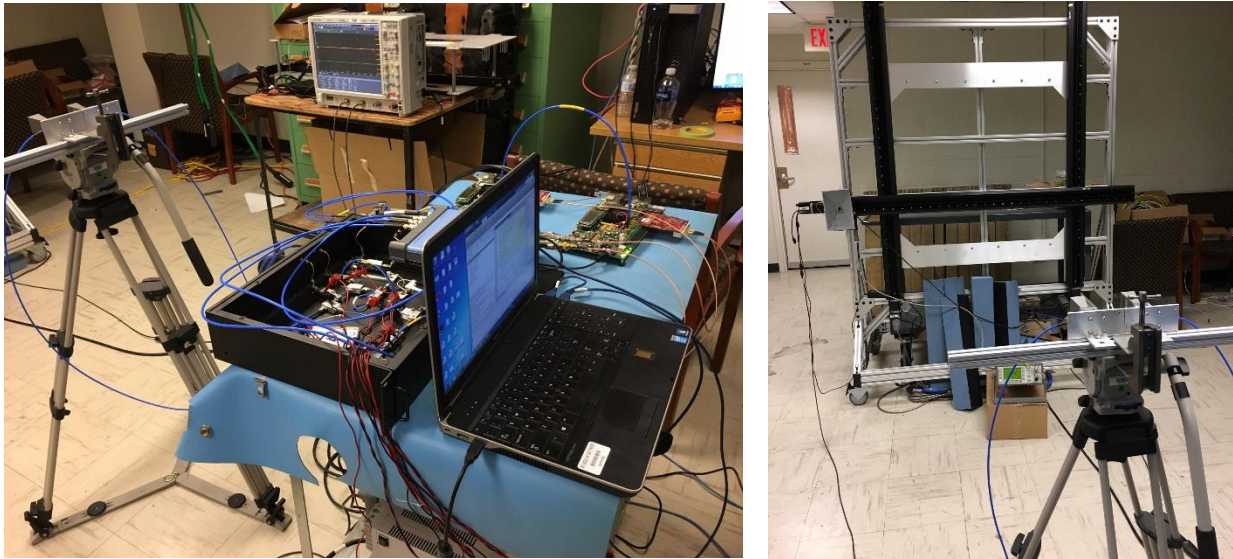


Figure 32. Waveform generation and transmission (left) with laptop, two VC707 board and RF upconverter and calibration hardware in black chassis and feedback loop (right) with Zaber Motorized Rail, two horn antennas and receiver antenna

4.1 Verification Results

Prior to collecting data, we had to verify that our test system was functioning as desired. The first step was ensuring that the FIR filtering in our FPGA design was outputting filtered waveforms as expected. In order to simulate the FIR, MATLAB generated a $4 \mu\text{s}$ sine wave and sent it to the FPGA. The data were then stored in an off-chip DDR send-buffer memory location and sent to the FIR by the DMA. The FIR outputted data were received by the DMA and stored in an off-chip DDR receive-buffer memory location. The FPGA then sent the receive-buffer data back to MATLAB. Figure 33 demonstrates the working FIR filter for $\frac{1}{3}$ sample delay and advance as well as a baseline wave with no delay or advance after inputting a 200 MHz sine wave.

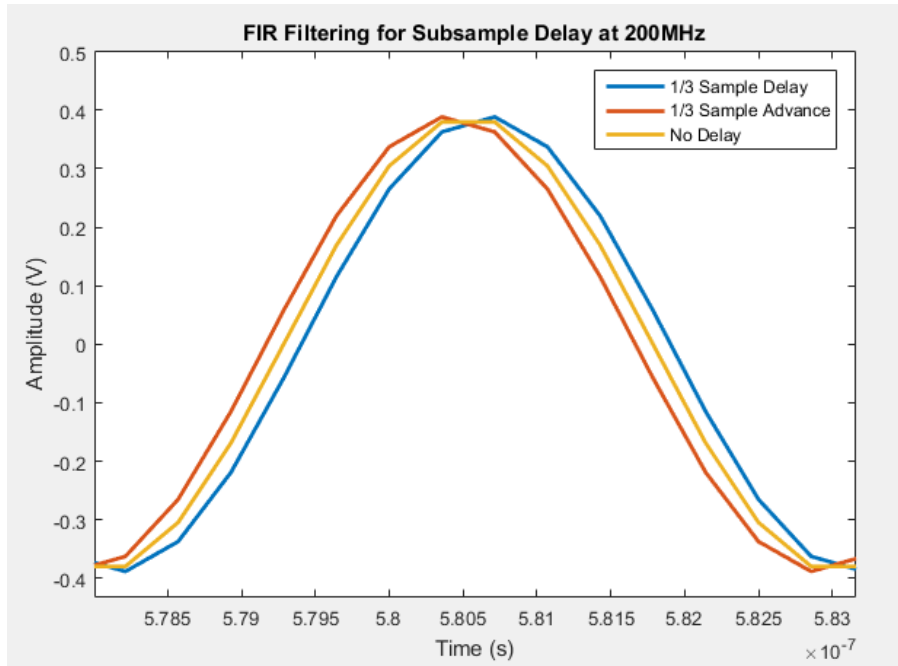


Figure 33. Single period of FIR filtered output for 1/3 sample delay, no delay or advance and 1/3 sample advance

The second step was ensuring that our upconverter design was converting our 400-800 MHz IF band up to 16.6-17 GHz Ku band successfully. We used a Keysight Technologies N9344C Handheld Spectrum Analyzer to run a spectrogram on the upconverter output in order to ensure that it was attenuating spurs with low jitter as desired; Figure 34 highlights a spectrogram of the functioning upconverter bringing 600 MHz up to 16.8 MHz.

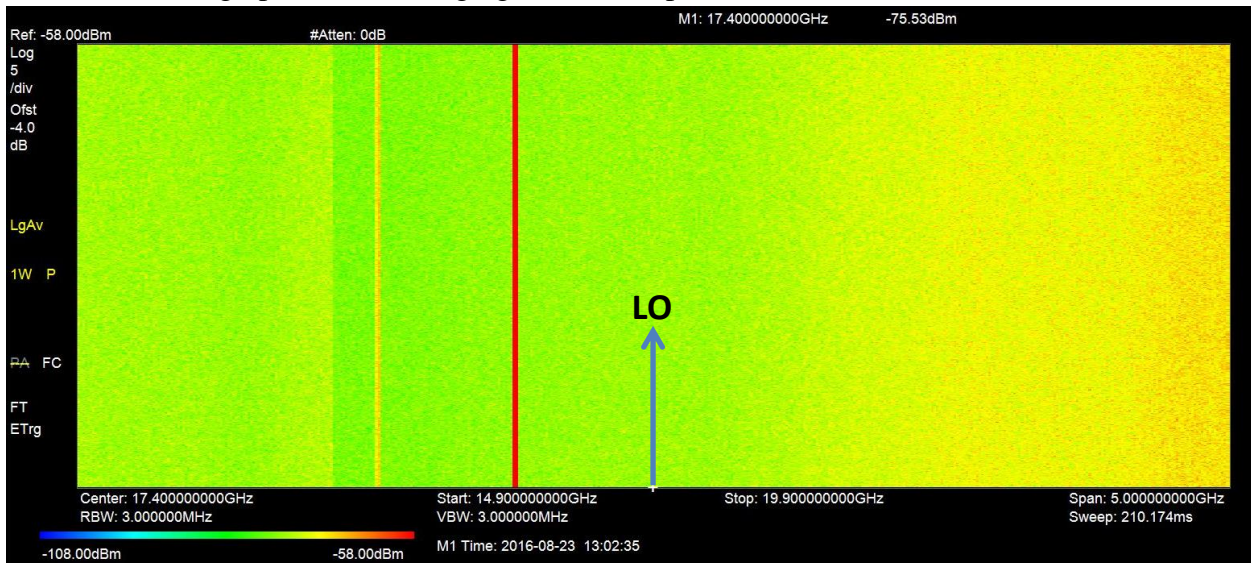


Figure 34. Spectrogram at 17.4 GHz (LO) center frequency with desired 16.8 GHz RF frequency (red) and 16.2 GHz second-order spur (yellow) highly attenuated

The third step was ensuring synchronization between our two FPGAs given that the eventual data collection relied heavily on phase alignment of outputted waveforms between the two FPGAs. Using a Keysight MS09404-A High-Speed Oscilloscope, we captured and analyzed the outputted waveforms of the two FPGAs. With a master FPGA triggering a slave FPGA, the outputted waveforms would have some time offset between them purely from the amount of time it took for the trigger to occur. However, our synchronization only required phase alignment between the two channels because we were able to control when we sampled the phase detector output and radiation patterns for data. Figure 35 gives an 18 μ s wideview of the synchronized waveforms while Figure 36 gives a close view.

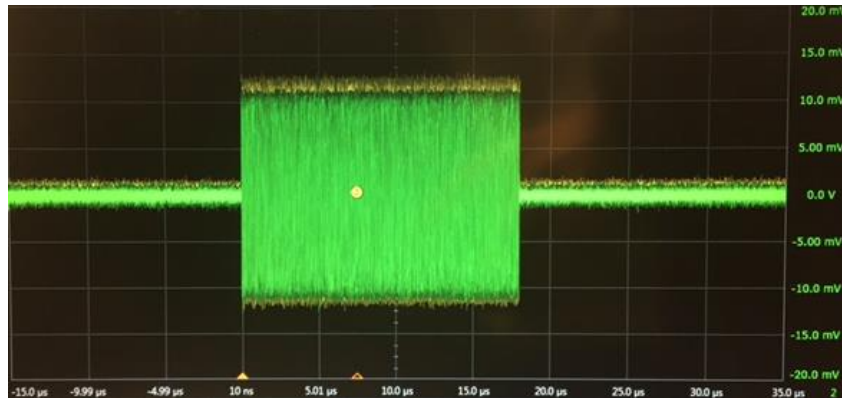


Figure 35. Oscilloscope wide view of synchronized FPGA outputs for 18 μ s waveform duration of master (green) and slave (yellow) transmitted signals

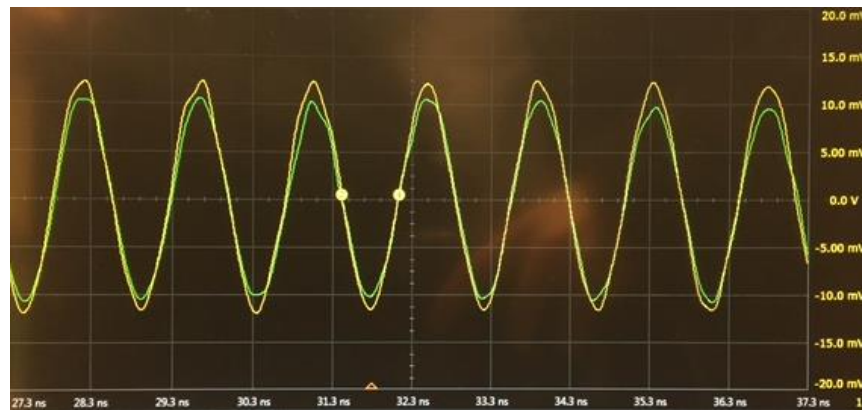


Figure 36. Close view (1ns/div) of phase aligned synchronization within 1ns between master (green) and slave (yellow) transmitted signals

The final step prior to beginning data collection was checking the environment of the antenna/receiver feedback loop. While the idea of inducing an interferometer works in theory, we needed to check that it was a possibility in our test environment, specifically verifying that the antennas would create a distinctive and easily trackable broadside null. Using the receiver antenna mounted on a Zaber Technologies A-LST0750B-E01 motorized linear rail, we took a 1D horizontal scan of the received power; Figure 37 demonstrates the interferometer antenna pattern in our test environment.

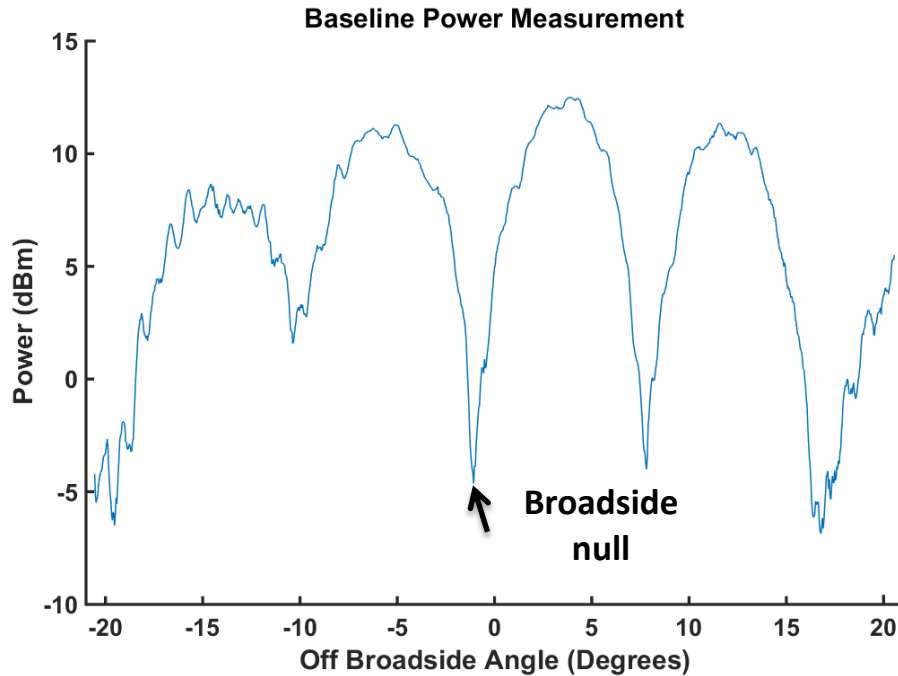


Figure 37. Received power measurement to prove interferometer concept in test environment

The test environment was not an anechoic near-field chamber and as a result, multi-path effects were clearly visible in our measurement. However, the main concern of our feedback loop was tracking the broadside null, which the multi-path did not significantly impact.

4.2 Experimental Results

After we had verified that the test system was ready for the experiment, we began collecting data. The first step was to establish a baseline null angle and transmit signal phase offset, as well as running consecutive tests over time and from full system resets to investigate the accuracy and consistency of the phase detector output. Figure 38 shows the antenna pattern of the baseline that we established.

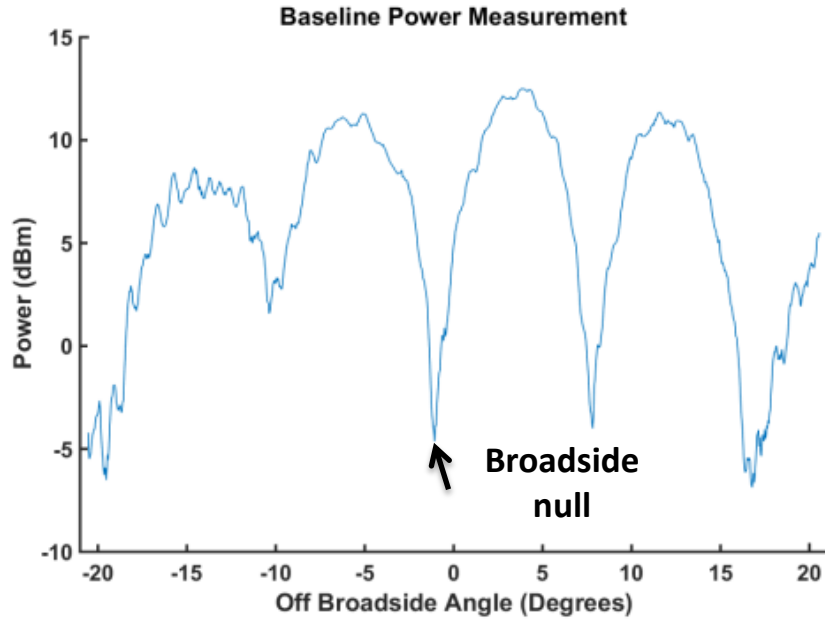


Figure 38. Baseline antenna pattern with broadside null at -1.16° off broadside angle

While an ideal interferometer would produce a deep broadside null at 0° off broadside angle, we tried to get our broadside null as close to 0° as possible. The fact that we did not get exactly 0° was not significant, as we were simply establishing a baseline null position to refer to when analyzing the consistency and accuracy of the DUT. Figure 39 shows the baseline phase detector output over 1000 measurements, highlighting the consistency of the calibration module.

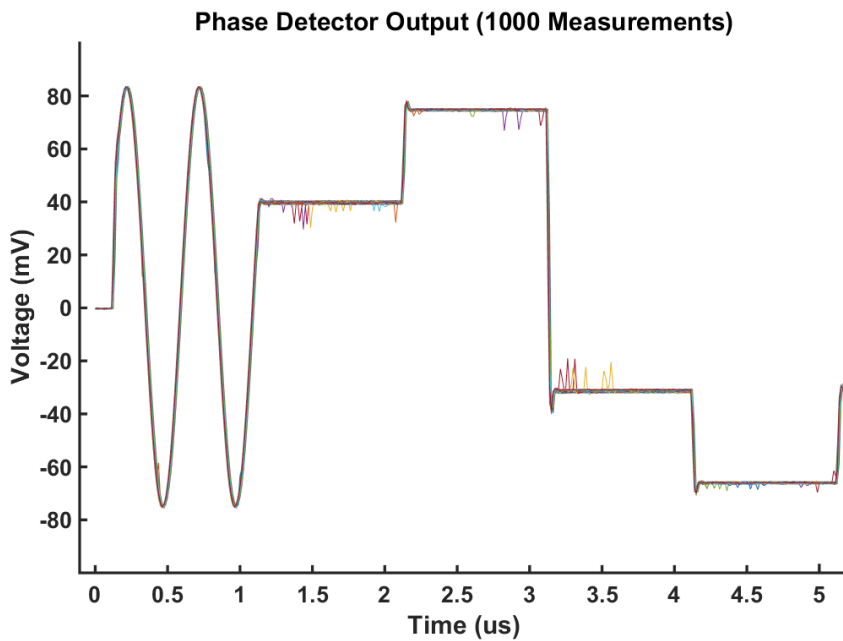


Figure 39. Baseline phase detector output over 1000 700 MHz calibration waveform measurements resulting in a calculated phase offset of -51.683°

We ran 1000 measurements over 5 full system resets and got very similar phase detector output and baseline power measurement. While there is some noise in Figure 39 at each DC voltage, the noise was not significant in the transmit signal phase offset calculation as each voltage level was averaged prior to the calculation. Figure 40 depicts a histogram of the actual baseline transmit signal phase offset calculations and their consistency.

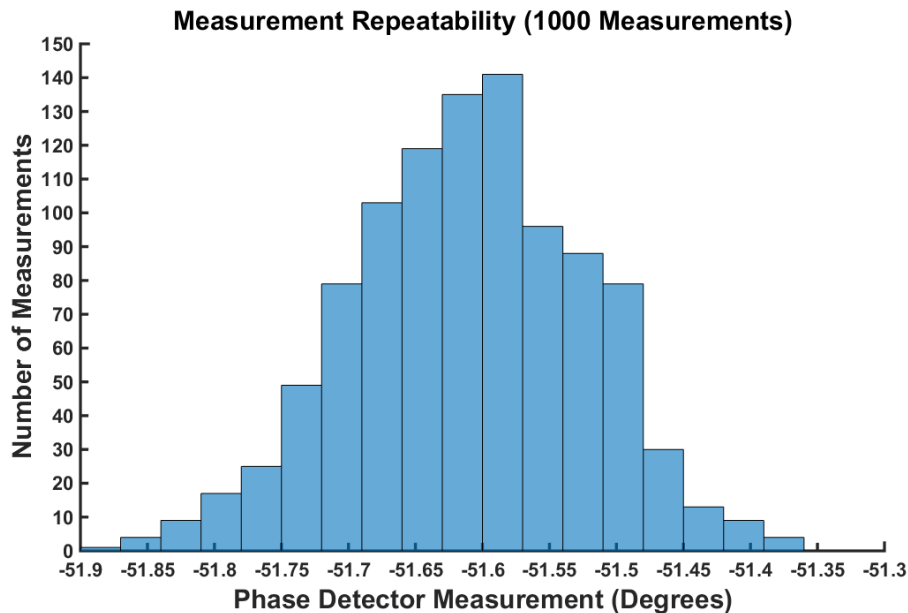


Figure 40. Baseline calculated transmit signal phase offset consistent within $\sim 1^\circ$ over 1000 measurements

As shown in Figure 40, the phase detector output is consistent within $<1^\circ$ over 1000 measurements from full system reset. Having established consistency of the calibration output as well as a baseline null angle and transmit signal phase offset, our next step was to apply external phase offsets using an analog phase shifter in order to investigate the accuracy of getting back to our baseline null angle and transmit signal phase offset relying solely on the calibration data. The accuracy is of concern as the ARTB will rely solely on the calibration data to guide the transmission of waveforms back to full synchronization, without any additional radiation pattern feedback loop. After applying an external phase offset, we first sent the calibration waveforms and analyzed the phase detector output, as shown in Figure 41.

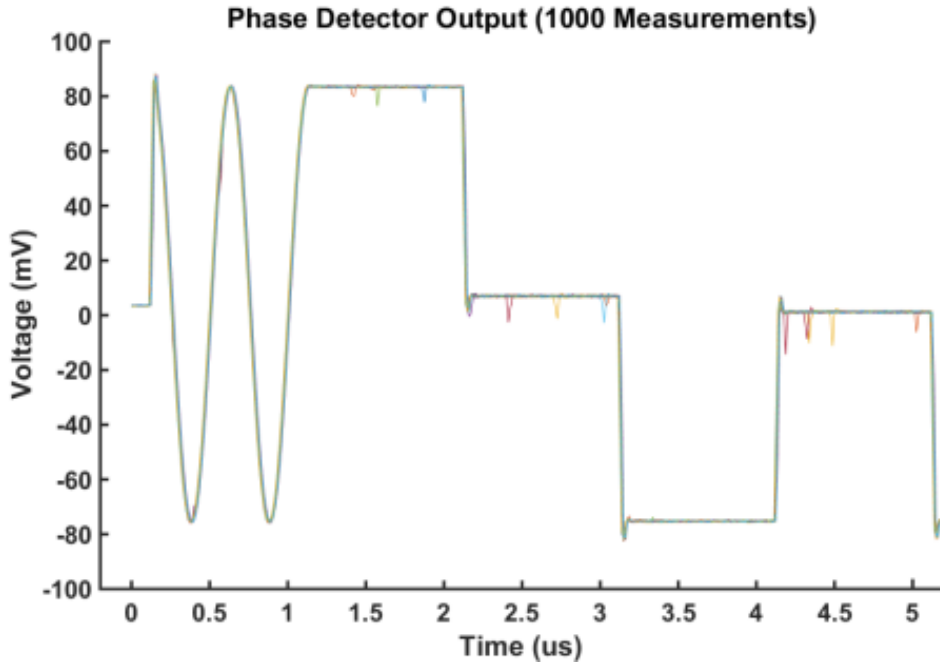


Figure 41. Initial phase detector output as a result of external phase offset applied by phase shifter

As expected, the phase detector output was different than the baseline phase detector output. From here, we calculated the new phase offset in order to determine how to appropriately time-align the waveforms, solely relying on the calibration data. We took initial power measurements as well to highlight the before and after effect of the broadside null; Figure 42 shows a sample initial power measurement prior to an external phase offset.

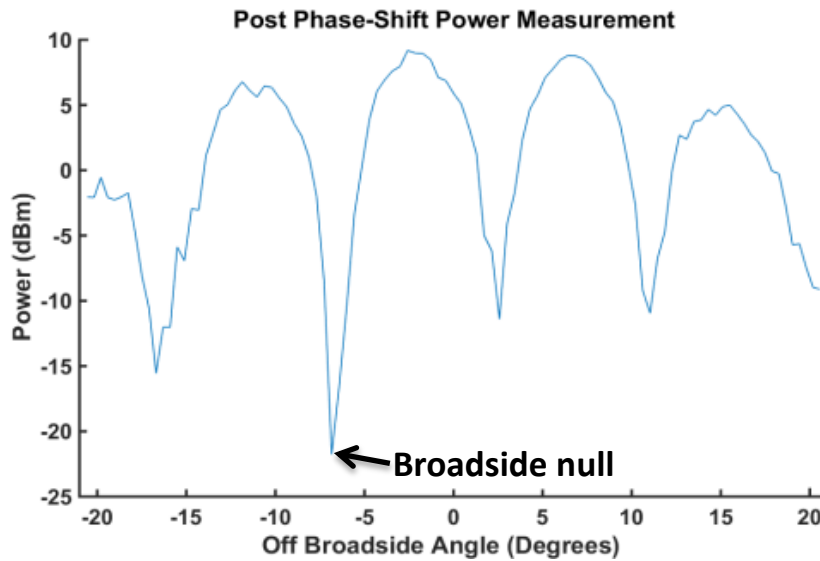


Figure 42. Initial power measurement as a result of external phase offset applied by phase shifter

With the baseline transmit signal phase offset established in the first step, and an initial transmit signal phase offset calculated after applying an external phase shift, we tuned the “test”

channel in order to account for the difference between the two offsets. By doing so we were effectively exploring the accuracy of the calibration module, investigating how close we could get back to the baseline null angle. We tested accuracy of the calibration module over 11 different external phase offsets spanning -180° to $+180^\circ$ in increments of $\sim 33^\circ$ increments; Figure 43 highlights the comparison between initial, resulting and baseline transmit signal phase offset over each applied phase offset.

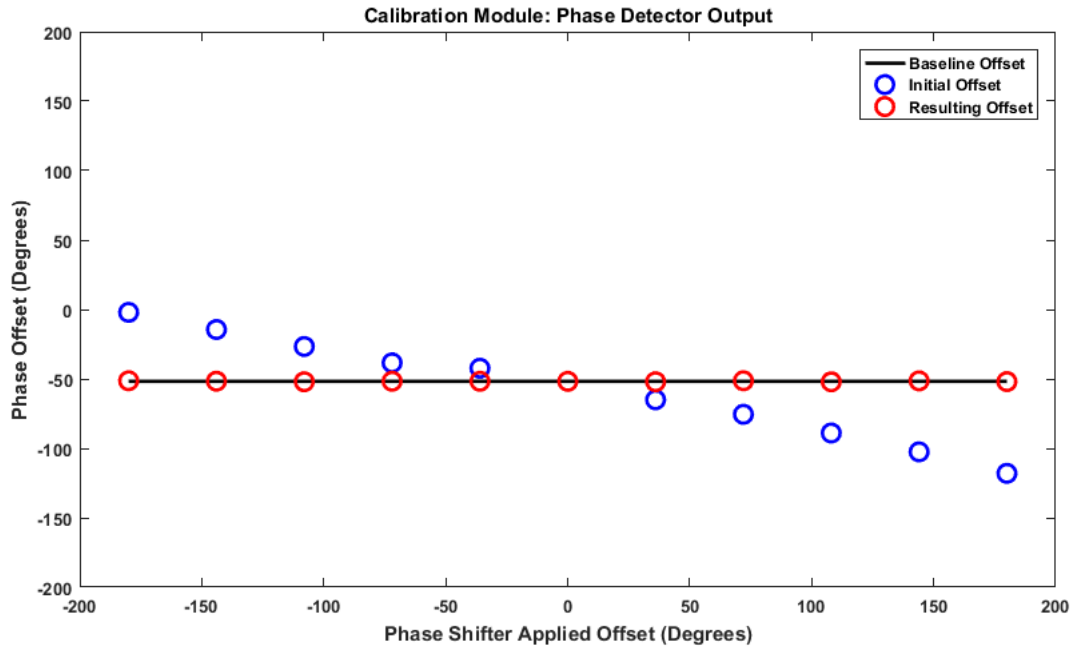


Figure 43. Phase detector calculated transmit signal offset over 11 distinct external phase offsets applied by phase shifter

The black line in Figure 43 represents the baseline transmit signal phase offset established in the first step, of -51.683° . The blue circles represent the initial calculated transmit signal phase offset after the external phase shift had been applied. The red circles represent the resulting calculated transmit signal phase offset after the “test” channel had been tuned to compensate for the offset between the blue circles and the black baseline transmit signal offset. We were able to achieve accuracy within $<1^\circ$ between the baseline transmit signal offset and resulting transmit signal offset.

However, the metric we truly cared about is how the compensation translated in terms of achieving the baseline null angle, as illustrated in Figure 44.

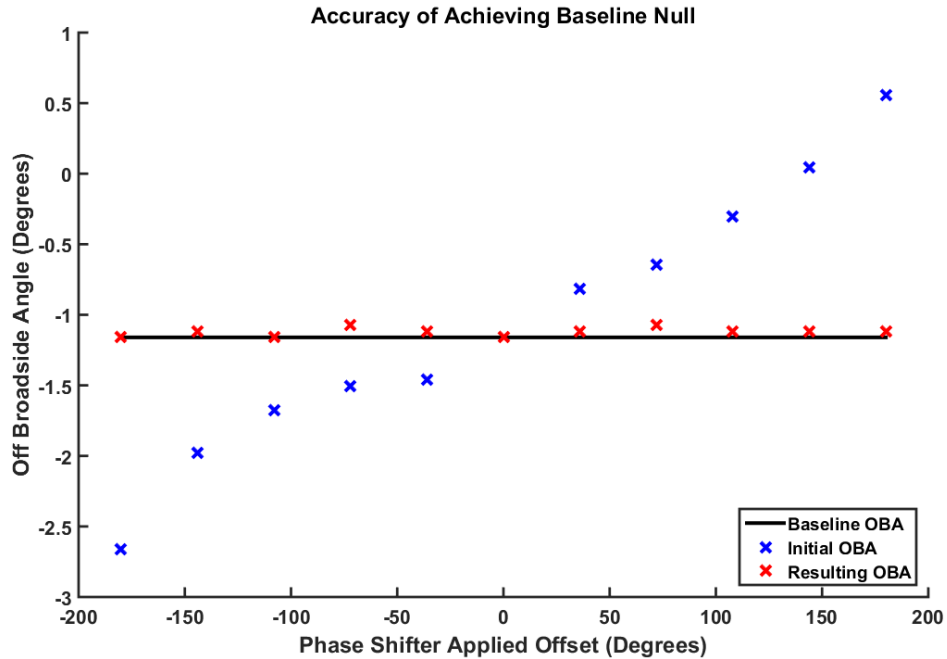


Figure 44. Comparison of initial null angle (blue) after applied phase shifter versus recalibrated null angle (red) based on calibration phase offset data

Again, the black line in Figure 44 represents the baseline null angle established in the first step, of -1.617° off broadside angle. The blue marks represent the initial broadside null angle, recorded solely for comparison, after the external phase shift had been applied. The red marks represent the resulting broadside null angle after the “test” channel had been tuned. Accuracy within $<1^\circ$ in phase offset translated to accuracy within 0.15° in terms of off broadside angle.

5. Discussion

The two sets of data collected in our test consisted of the calculated transmit signal phase offsets from the calibration phase detector output, and the 1D horizontal power scans of the radiated interference patterns. The first step in analyzing our data was to investigate the implication of the results. The second step was to highlight possible areas of concern that may have affected the results significantly.

5.1 Implication of Results

Given the measured data concerning the ability of the calibration system to account for external phase offsets, it is possible to come to conclusions concerning whether the calibration system appropriately meets the system requirements for ensuring that the beam pattern is directed at the desired angle. The primary requirement for the system is that the calibration between time-steered channels is not the limiting factor in the testbed's beam steering ability. The other components which are used to steer the beam are the phase shifters for each element within the AESA panels. These phase shifters have 6 bit phase resolution, allowing for phase resolution to 5.625° . As the calibration system was able to correct for the phase difference between the test and reference channels within 1° , we do not believe that the calibration system is the limiting factor of the system. One qualification to claiming that the calibration system is not the limiting factor of the system is that the single frequency experiment does not predict the correction consistency of achieving a wideband null over the full system bandwidth. Given the frequency independence of the accuracy of phase measurements from the calibration module, we do not expect testing over the full system bandwidth to dramatically alter the accuracy and consistency of achieving a desired beam angle, but the calibration module would require additional verification for complete assurance.

5.2 Possible Data Concerns

A few concerns arose while interpreting the data related to the testing setup and environment. Two such considerations were the viability of performing a horizontal linear scan as opposed to a curved scan, and the multipath effects of the testing room where the measurements were taken. In this section we will investigate these concerns and show that their effects do not negatively alter the results and conclusions of the experiment.

5.2.1 Horizontal Linear Scan

During the course of the project, the decision to use a horizontal linear scan for recording the power measurements was brought up as a possible concern, as the distance between the transmission and receiver antennas is larger at the edges of the scan. As depicted in Figure 45, given the full scan angle and the distance of 2 meters between the transmission and receiver antennas, the largest extent of this difference in distance was calculated to be 136 mm at the scan edge.

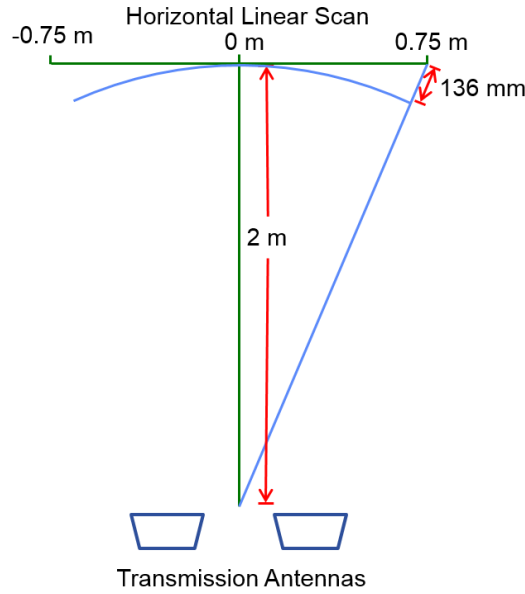


Figure 45. Horizontal Linear Scan Measurement Distance vs. Curved Scan

Two alternatives to the chosen scan method would have been possible to counteract this difference in distance. A curved scan as depicted in Figure 45 would allow the receiver antenna to maintain a constant 2 meter distance from the transmission antennas, but would also require hardware to perform a curved scan, or manual positioning of the receiver. The other alternative would be to rotate the tripod head which held the transmission antenna setup while keeping the receiver antenna in a constant position. This method would have also required manual rotation to take each successive measurement. Both of these would dramatically increase the measurement time and reduce the accuracy of measurement location, adding in the potential for operator error. As such, the horizontal scan remained the most attractive measurement for the test.

The decision to perform the test with the linear scan required analysis of the system geometry to ensure that the difference in distance at the edges of the scan did not negatively affect the resultant data. At the worst case, the distance differential was calculated to be 136 mm. Given the 16.7 GHz test frequency that was employed, the wavelength (calculated to be 17.964 mm) was determined to be sufficiently small for a significant phase difference between the ideal curved measurement and the linear scan measurement; 7.57 wavelengths of the transmitted tone would occur between the two. Therefore, the difference in distance would dramatically affect any phase measurements taken. For the purposes of aligning the null power positions however, the phase of the signal at the receiver is not important.

The other possible implication of the difference in distance between the center and edges of the measurement scan is the free space power loss. Given the Friis Equation represented in equation 14, it is possible to determine the power loss over the 136 mm distance in relation to the power at the center of the scan.

$$P_r = P_t + G_t + G_r + 20 \log \left(\frac{\lambda}{4\pi\Delta r} \right) \quad (14)$$

In equation 14, P_t = transmitted power, G_t = transmitter gain, G_r = receiver gain, Δr = distance between the antennas, $\lambda = 2\pi/f$ where f = frequency, and P_r = received power. As the

136 mm distance is very small, the power loss was calculated to be 0.1 dB. The 0.1 dB loss was determined not to be substantial for the power measurement especially because we were only measuring the broadside null angle. As such the horizontal linear scan was deemed accurate for the conclusions reached through this experiment.

5.2.2 Multipath effects

One other concern which arose throughout the experiment involved the multipath effects of the testing environment. It was evident early within the testing period that the physical geometry and layout of the testing room induced reflection effects which interfered with the signal measurement at the receiver antenna. The multipath interference is reflected in Figure 46 which shows the results of all the final null location measurements from the return-to-baseline tests.

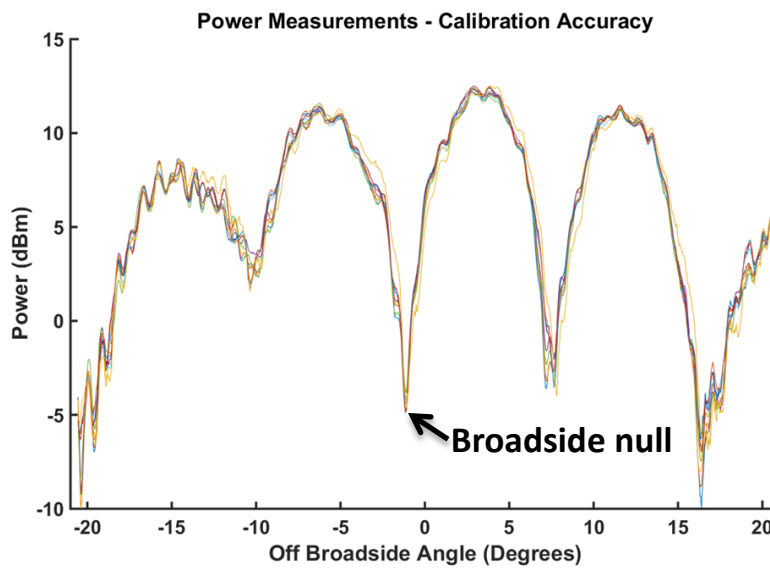


Figure 46. Overlaid return-to-baseline power scan measurements

The multipath effects are most notable on the edges of the scan region, where there is more interference from the walls of the testing environment and other objects within the room. Fortunately, the effects of the multipath interference were consistent throughout the testing period, as the room layout was not changed between tests. The consistency of the effects is represented in Figure 46; the return-to-baseline test measurements were taken at different times throughout the testing period, and the interference pattern was observed to be the same over all of the tests. Furthermore, the multipath effects did not inhibit our ability to identify the location of the broadside null from the power measurement or use the phase data gathered from the calibration module to re-align the null at the baseline position. It was therefore determined that although it would be beneficial to carry out additional testing in an anechoic chamber in the future, the testing environment was appropriate for the experiment outlined in this report.

6. Conclusions

6.1 Measurement Conclusions

Through analysis of the gathered results and the testing system, it was determined that the ARTB calibration system was able to accurately and consistently provide phase difference data to account for an external offset and align the beam pattern with the desired baseline. This conclusion was reached as the ability to use the ARTB calibration system to account for external offset was determined not to be the limiting factor of the beam steering capabilities of the Airborne Radar Testbed antenna system.

6.2 Future Steps

Given an extended testing period, it would be beneficial to gather additional data to more fully characterize the behavior of the Airborne Radar Testbed's calibration system. The first additional experiment would be to perform the same test as described in this report within an anechoic chamber, something which was not possible during this project due to scheduling and timing constraints with the near-field chamber at Lincoln Laboratory. Testing in an anechoic chamber would eliminate the multipath behavior observed in the measured power scan data and provide additional assurance that the multipath interference did not negatively affect the results of the experiment.

Beyond carrying out the same test in an anechoic chamber, it would also be beneficial to test at wider bandwidths. The test at a single frequency of 16.7 GHz (700 MHz IF) provided an understanding of the accuracy and consistency of the phase measurement performed by the calibration system and the ability to use this measurement to return to a baseline beam angle, but for a single frequency, phase and time-delay are essentially the same, as the frequency dependence of phase shift is constant for a single frequency. As a result, using the phase detector measurement to re-align the baseline null angle at a single frequency does not mean that the null angle is properly aligned for the other frequencies within the transmission band. Testing at wider bandwidths, the transmit signal phase offset measurements would be taken in the same way as they were for a single frequency: by sending frequency specific calibration waveforms and measuring the transmit signal phase offset between the two channels.

The foundation for the full bandwidth experiment is already developed through the FPGA design that was created for the experiment described within this report. The FIR filters developed support both sub-sample time delay control as well as continuous phase control, allowing for the necessary corrections to re-align a wideband null to a recorded baseline.

Along with the wider bandwidth test, full characterization of the calibration system would require an understanding of the effects of the environmental conditions on the system's ability to properly calibrate the antenna array system. As the system will eventually be employed on a Twin Otter aircraft, it will be subject to temperature variation as well as vibration throughout a flight. Understanding the implications of these environmental conditions would allow for conclusions to be reached regarding how often the system would need to be calibrated

using the calibration system, or if a single calibration before flight to account for startup offsets would be sufficient.

Works Cited

- Coleman, C. (2004). *An Introduction to Radio Frequency Engineering* (86-108). Cambridge, United Kingdom: Cambridge University Press. Print.
- Davis, A. & Agarwal, K. (2001) *Radio Frequency Circuit Design* (271-274). New York, NY: John Wiley & Sons, Inc. Print.
- Longbrake, M. (2012). True Time-Delay Beamsteering for Radar. *IEEE National Aerospace and Electronics Conference (NAECON)*, 25–27 July, 246–249. Retrieved from <http://ieeexplore.ieee.org/document/6531062/>
- Marvasti, F. A., ed. (2001). *Nonuniform sampling: Theory and practice* (842-852). New York, NY: Kluwer Academic/Plenum Publ. Print.
- Poornachandra, S. & Sasikala B. (2010). Design of FIR Filter - Windowing Techniques. In *Digital Signal Processing (FIR-32-FIR-49)*, 3rd Edition. West Patel Nagar, New Delhi: Tata McGraw Hill Education Private Limited. Print.
- Prabhu, K. M. (2014). Truncated Taylor Family. In *Window Functions and Their Applications in Signal Processing* (94-95). Boca Raton, FL: CRC Press. Print.
- Shannon, C. (1998). Communication in the Presence of Noise. *Proceedings of the IEEE*, 86(2), 447-457. (Reprinted from *Proceedings of the IRE*, 37, 10-21)
- Skolnik, M. (2008). *Radar Handbook*, 3rd Edition (1.1 – 13.7). The McGraw-Hill Companies, USA. Print.
- Välämäki, V. (1995). Discrete-Time Modeling of Acoustic Tubes Using Fractional Delay Filters. Ph.D. dissertation, Helsinki University of Technology, Helsinki, Finland. Retrieved from http://users.spa.aalto.fi/vpv/publications/vesan_vaitos/abstract.pdf

Appendix A. MATLAB Code for Scanning Zaber Rail and Taking Block Measurements

```
%Take Multiple Scans with Block Data Measurement at each Location:

instrreset;
fc=instrfindall;
if isempty(fc)==0;
    fclose(fc);
    delete(fc);
    clear fc;
end

%% Clear Command Window and Workspace

clc;
clear;

%% Variables to Change

NUMTESTS = 1;
PRESAMP = 10;           %number of samples to take before the trigger
NumUs = 20;            %number of microseconds of data to take at each
position
POSTSAMP = ceil(81*NumUs); %number of samples to take at each position
81(Samp/Us) * NumUs
TRIGGERCH = 2;         %trigger on channel B-(1)
AUTOTRIG = 0;         %set autotrigger timeout (0 for no autotrigger)

%% Initialize Zaber Rail

%conversion parameters
LSTmicrostepRev=0.124023438e-6; %LST rails
BLQmicrostepRev=4.21875e-6; %BLQ rails
microStepSec=1.6384; %BLQ SPEED
rdwait=.025; %Serial Port Delay

addr='COM58';
zaber=initzp(addr,1);
%uncomment these lines to manually move rail
% display('Enter any manual Zaber code or type return to continue:');
% keyboard
%fprintf(zaber,'/01 0 move abs 1500000'); %move to center

%% Load PicoScope Configuration Information

PS4000aConfig;

%% PicoScope Parameter Definitions

% Define any parameters that might be required throughout the script.

channelA = ps4000aEnuminfo.enPS4000AChannel.PS4000A_CHANNEL_A;
```

```

channelB = ps4000aEnuminfo.enPS4000AChannel.PS4000A_CHANNEL_B;
channelC = ps4000aEnuminfo.enPS4000AChannel.PS4000A_CHANNEL_C;
channelD = ps4000aEnuminfo.enPS4000AChannel.PS4000A_CHANNEL_D;

%% PicoScope Connection

% Create device - specify serial number if required
% Specify serial number as 2nd argument if required.
ps4000aDeviceObj = icdevice('picotech_ps4000a_generic', '');

% Connect device
connect(ps4000aDeviceObj);

%% Display PicoScope Unit Information

[infoStatus, unitInfo] = invoke(ps4000aDeviceObj, 'getUnitInfo');

disp(unitInfo);

%% Set PicoScope Channels

% Default driver settings applied to channels are listed below -
% use ps4000aSetChannel to turn channels on or off and set voltage ranges,
% coupling, as well as analogue offset.

% In this example, data is only collected on Channel A so default settings
% are used and channels B to H are switched off.

% Channels      : 1 - 7 (ps4000aEnuminfo.enPS4000AChannel.PS4000A_CHANNEL_B
- PS4000A_CHANNEL_H)
% Enabled       : 0
% Type         : 1 (ps4000aEnuminfo.enPS4000ACoupling.PS4000A_DC)
% Range        : 8 (ps4000aEnuminfo.enPS4000ARange.PS4000A_5V)
% Analogue Offset: 0.0

% Execute device object function(s)
[status.setChA] = invoke(ps4000aDeviceObj, 'ps4000aSetChannel', 0, 1, 1, 8,
0.0); %Power Reading
[status.setChB] = invoke(ps4000aDeviceObj, 'ps4000aSetChannel', 1, 1, 1, 3,
0.0); %Master Diode Detector
[status.setChC] = invoke(ps4000aDeviceObj, 'ps4000aSetChannel', 2, 1, 1, 3,
0.0); %Slave Diode Detector
[status.setChD] = invoke(ps4000aDeviceObj, 'ps4000aSetChannel', 3, 1, 1, 3,
0.0); %Mixer Output

%if(ps4000aDeviceObj.channelCount == PicoConstants.QUAD_SCOPE ||
ps4000aDeviceObj.channelCount == PicoConstants.OCTO_SCOPE)
% [status.setChC] = invoke(ps4000aDeviceObj, 'ps4000aSetChannel', 2, 0, 1,
8, 0.0);
% [status.setChD] = invoke(ps4000aDeviceObj, 'ps4000aSetChannel', 3, 0, 1,
8, 0.0);
%end

```

```

if(ps4000aDeviceObj.channelCount == PicoConstants.OCTO_SCOPE)

    [status.setChE] = invoke(ps4000aDeviceObj, 'ps4000aSetChannel', 4, 0, 1,
8, 0.0);
    [status.setChF] = invoke(ps4000aDeviceObj, 'ps4000aSetChannel', 5, 0, 1,
8, 0.0);
    [status.setChG] = invoke(ps4000aDeviceObj, 'ps4000aSetChannel', 6, 0, 1,
8, 0.0);
    [status.setChH] = invoke(ps4000aDeviceObj, 'ps4000aSetChannel', 7, 0, 1,
8, 0.0);

end

% Obtain the maximum ADC Count from the driver
maxADCCount = double(get(ps4000aDeviceObj, 'maxADCValue'));

%% Verify Timebase Index and Maximum Number of Samples

% Driver default timebase index used - use ps4000aGetTimebase2 to query the
% driver as to suitability of using a particular timebase index and the
% maximum number of samples available in the segment selected (the buffer
% memory has not been segmented in this example) then set the 'timebase'
% property if required.
%
% To use the fastest sampling interval possible, set one analogue channel
% and turn off all other channels.
%
% Use a while loop to query the function until the status indicates that a
% valid timebase index has been selected. In this example, the timebase
% index of 79 is valid.

% Initial call to ps4000aGetTimebase2 with parameters:
% timebase      : 0
% segment index : 0

status.getTimebase2 = PicoStatus.PICO_INVALID_TIMEBASE;
timebaseIndex = 0;
while(status.getTimebase2 == PicoStatus.PICO_INVALID_TIMEBASE)

    [status.getTimebase2, timeIntervalNanoSeconds, maxSamples] =
invoke(ps4000aDeviceObj, 'ps4000aGetTimebase2', timebaseIndex, 0);

    if(status.getTimebase2 == PicoStatus.PICO_OK)
        break;
    else
        timebaseIndex = timebaseIndex + 1;
    end
end

end

set(ps4000aDeviceObj, 'timebase', timebaseIndex);

%% Set Simple Trigger
% Set a trigger on Channel A, with an auto timeout - the default value for

```

```

% delay is used.

% Trigger properties and functions are located in the Instrument
% Driver's Trigger group.

triggerGroupObj = get(ps4000aDeviceObj, 'Trigger');
triggerGroupObj = triggerGroupObj(1);

% Set the autoTriggerMs property in order to automatically trigger the
% oscilloscope after 1 second if a trigger event has not occurred. Set to 0
% to wait indefinitely for a trigger event.

set(triggerGroupObj, 'autoTriggerMs', AUTOTRIG);

% Channel      : 0 (ps4000aEnuminfo.enPS4000AChannel.PS4000A_CHANNEL_A)
% CHANGE THIS TO TRIGGER ON THE ENVELOPE CHANNEL
% Threshold    : 10 (mV)
% Direction    : 2
(ps4000aEnuminfo.enPS4000AThresholdDirection.PS4000A_RISING)

[status.setSimpleTrigger] = invoke(triggerGroupObj, 'setSimpleTrigger',
TRIGGERCH, 5, 2);

%% Set PicoScope Block Parameters

% Capture a block of data and retrieve data values for Channel A.

% Block data acquisition properties and functions are located in the
% Instrument Driver's Block group.

blockGroupObj = get(ps4000aDeviceObj, 'Block');
blockGroupObj = blockGroupObj(1);

% Set pre-trigger and post-trigger samples as required
% 10 presamples and POSTSAMP postsamples

set(ps4000aDeviceObj, 'numPreTriggerSamples', PRESAMP);
set(ps4000aDeviceObj, 'numPostTriggerSamples', POSTSAMP);

%% Scan and Measure

%comparizon values used for direction selection
left = 'left';
right = 'right';
initdir = right;

%prompt the user to select initial direction
%initdir = input('Choose a direction (left or right): ');

%initialization settings for step size and maximum X value
XMaxVal = 3000000;

%User selection of the stepsize

```

```

stepInput = input('Choose a step size (% of total): ');
stepSize = stepInput*XMaxVal/100;

%Create X Position Vector and Off Broadside Angle Vector
xpos = (-0.75:(1.5/(100/stepInput)):0.75);
oba = atan(xpos/2); %xpos is the distance from the geometric mean between
                    %the two antennas in meters, 2 is the distance from
                    %the antenna to the probe

%depending on user-selected direction (preset to 'right' for now)
%move to the initial position
if (strcmp(initdir, 'left'))
    nextpos = XMaxVal;    %left
    otherdir = 'right';
else
    nextpos = 0;          %right
    otherdir = 'left';
end
nextposstr = num2str(nextpos);
str = horzcat('/01 0 move abs ', nextposstr);
fprintf(zaber, str);
%wait until the zaber gets to the start position

fprintf(zaber, '/01 0 get pos');
[an1,Cnt,TOMsg]=fscanf(zaber);
lennextpos = numel(num2str(nextpos));
currentpos = an1(length(an1)-10:length(an1)-2);
while(strcmp(currentpos, 'IDLE -- 0')~=1)
    fprintf(zaber, '/01 0 get pos');
    [an1,Cnt,TOMsg]=fscanf(zaber);
    currentpos = an1(length(an1)-10:length(an1)-2);
end

%Moved to starting position, ready to begin test
;
power(1:(XMaxVal/stepSize),1:PRESAMP+POSTSAMP,1:NUMTESTS) = 0;
ChB(1:(XMaxVal/stepSize),1:PRESAMP+POSTSAMP,1:NUMTESTS) = 0;
ChC(1:(XMaxVal/stepSize),1:PRESAMP+POSTSAMP,1:NUMTESTS) = 0;
ChD(1:(XMaxVal/stepSize),1:PRESAMP+POSTSAMP,1:NUMTESTS) = 0;

for testNum = 1:NUMTESTS
    if (mod(testNum,2) == 0) %when even, move in the opposite direction
        dir = otherdir;
    else
        dir = initdir;      %when odd, move in the initial direction
    end

    %moving to start position
    if (strcmp(dir, 'left'))
        nextpos = XMaxVal;    %left
        otherdir = 'right';
        initialmovenextpos = 'IDLE -- 3000000';
        nextmovenextpos = 'IDLE NI 3000000'; %sometimes this is returned when
the probe gets to the end?
    else
        nextpos = 0;          %right

```

```

        otherdir = 'left';
        initialmovenextpos = 'IDLE -- 0';
        nextmovenextpos = 'IDLE NI 0'; %sometimes this is returned when the
probe gets to the end?
    end
    nextposstr = num2str(nextpos);
    str = horzcat('/01 0 move abs ', nextposstr);
    fprintf(zaber, str);
    %wait until the zaber gets to the start position

    fprintf(zaber, '/01 0 get pos');
    [an1,Cnt,TOMsg]=fscanf(zaber);
    currentpos = an1(length(an1)-numel(initialmovenextpos)-1:length(an1)-2);

    while(strcmp(currentpos, initialmovenextpos) ~= 1 && strcmp(currentpos,
nextmovenextpos) ~= 1)
        fprintf(zaber, '/01 0 get pos');
        [an1,Cnt,TOMsg]=fscanf(zaber);
        currentpos = an1(length(an1)-numel(initialmovenextpos)-1:length(an1)-
2);
    end

    %Moved to starting position, ready to begin test (uncomment next line to
%have system wait for user input on every scan)
    %input ('Moved to starting X position, press enter to continue: ');
    %probe is in initial position, read first power level from picoscope
    [status.runBlock] = invoke(blockGroupObj, 'runBlock', 0);
    [POSTSAMPles, overflow,
power(1,1:PRESAMP+POSTSAMP,testNum),ChB(1,1:PRESAMP+POSTSAMP,testNum),ChC(1,1
:PRESAMP+POSTSAMP,testNum),ChD(1,1:PRESAMP+POSTSAMP,testNum)] =
invoke(blockGroupObj, 'getBlockData', 0, 0, 1, 0);

    for i = 1:(XMaxVal/stepSize)
        if (strcmp(dir, 'left'))
            nextpos = XMaxVal-(stepSize*i);          %left
        else
            nextpos = stepSize*i;                    %right
        end
        nextposstr = num2str(nextpos);
        str = horzcat('/01 0 move abs ', nextposstr);
        fprintf(zaber, str);

        %check if it has gotten there yet, wait until it gets there

        fprintf(zaber, '/01 0 get pos');
        [an1,Cnt,TOMsg]=fscanf(zaber);
        lennextpos = numel(num2str(nextpos));
        currentpos = str2double(an1(length(an1)-lennextpos-1:length(an1)-1));

        while(currentpos ~= nextpos)

            fprintf(zaber, '/01 0 get pos');
            [an1,Cnt,TOMsg]=fscanf(zaber);
            currentpos = str2double(an1(length(an1)-lennextpos-1:length(an1)-
1));

```

```

    end
    %probe is in position, read power from picoscope
    [status.runBlock] = invoke(blockGroupObj, 'runBlock', 0);
    [POSTSAMPles, overflow,
power(i+1,1:PRESAMP+POSTSAMP,testNum),ChB(i+1,1:PRESAMP+POSTSAMP,testNum),ChC
(i+1,1:PRESAMP+POSTSAMP,testNum),ChD(i+1,1:PRESAMP+POSTSAMP,testNum)] =
invoke(blockGroupObj, 'getBlockData', 0, 0, 1, 0);
    end

    powerdBm = (log(power/110.1)/0.1211); %%these values result from the
curvefit of the mV to dBm plot
    for i = 1:numel(powerdBm)
        if(powerdBm(i) == -Inf)
            powerdBm(i) = 0;
        end
    end
end

%flip every even numbered test (as the test is taken left to right, the
%data is reversed (may also need to take negative of nullAngle)
for i = 1:NUMTESTS
    if (mod(i, 2) == 0) %even
        powerdBm(i,:) = fliplr(powerdBm(i,:));
    end
end

%% Disconnect Devices

% Disconnect device object from hardware.
disconnect(ps4000aDeviceObj);
delete(ps4000aDeviceObj);
instrreset;
fc=instrfindall;
if isempty(fc)==0;
    fclose(fc);
    delete(fc);
    clear fc;
end

%% Plot Gathered Data

timeNs = double(timeIntervalNanoSeconds) * double(0:PRESAMP+POSTSAMP - 1);
timeUs = timeNs / 1e3;

%%plot power vs x-position
%plot(xpos, power)
%title('Received Power - Horizontal Slice');
%xlabel('Position (m)');
%ylabel('Voltage (mV)');

%%curve fitting
%figure
%plot(xpos, powerdBm)
%title('Received Power - Horizontal Slice');
%xlabel('Position (m)');

```

```

%ylabel('Power (dBm)');

%figure
%plot(oba, powerdBm)
%xlim([-21 21])
%title('Received Power - Horizontal Slice');
%xlabel('Off Broadside Angle (Degrees)');
%ylabel('Power (dBm)');

%% Pull 1d Power Scan from Block Data
sizedata = size(powerdBm);
scandata(1:sizedata(1)) = 0;
for i = 1:sizedata(1)
    scandata(i) = mean(powerdBm(i,800:1400));
end

figure(2)
plot(oba, scandata)
xlim([-21 21])
title('Received Power - Horizontal Slice');
xlabel('Off Broadside Angle (Degrees)');
ylabel('Power (dBm)');

save('ChC.mat', 'ChC');
save('ChD.mat', 'ChD');
save('power.mat', 'power');
save('powerdBm.mat', 'powerdBm');
save('oba.mat', 'oba');
save('timeUs.mat', 'timeUs');
save('scandata.mat', 'scandata');

```